Haberlie Alex (Orcid ID: 0000-0001-9172-4028)

Mean Storms: Composites of Radar Reflectivity Images During Two Decades of Severe Thunderstorm Events

Short Title: Mean Radar Composites of Severe Thunderstorm Events

ALEX M. HABERLIE*[1], WALKER S. ASHLEY[2], MARISA R. KARPINSKI[1]

[1]*Department of Geography and Anthropology, Louisiana State University, Baton Rouge, LA, U.S.A.*

[2]*Department of Geographic and Atmospheric Sciences, Northern Illinois University, DeKalb, IL, U.S.A*

This is the author manuscript accepted for publication and has undergone full peer review but has not been through the copyediting, typesetting, pagination and proofreading process, which may lead to differences between this version and the Version of Record. Please cite this article as doi: 10.1002/joc.6804

*Corresponding Author Address: Department of Geography and Anthropology, Louisiana State University, Baton Rouge, LA 70803

Email: ahaberlie1@lsu.edu

ABSTRACT

This research quantifies the spatiotemporal statistics of composite radar reflectivity in the vicinity of severe thunderstorm reports. By using over 20 years (1996 – 2017) of data and 500,000 severe thunderstorm reports, this study presents the most comprehensive analysis of the mesoscale presentation of radar reflectivity composites during severe weather events to date. We first present probability matched mean composites of approximately 5,000 radar images centred on tornado reports that contain one of three types of manually-labelled convective storm modes—namely, 1) quasi-linear convective system (QLCS); 2) cellular; or 3) tropical system. Next, we generate composites for tornado report data stratified by EF-scale and for four temporal periods during which notable severe weather events took place. The data are then stratified by hazard, region, season, and time of day. The results show marked spatiotemporal and intra-hazard variability in radar presentation. In general, cellular convection is favoured in the Great Plains of the U.S, whereas QLCS convection is favoured in the Southeast U.S. Night and cool-season subsets showed a preference for QLCS convection, whereas day and warm-season subsets showed a preference for cellular convection. These results agree well with the existing literature and suggest that the data extraction and organization approach is sound. Because of this, these data will be useful for future image classification studies in climate and atmospheric sciences—particularly those involving storm mode classification.

Keywords: Weather Radar, Severe Weather, Radar Climatology

1. Introduction

Severe thunderstorm events are responsible for many weather-related injuries, deaths, and billion-dollar-losses in the United States (Ashley 2007; Black and Ashley 2010; Schoen and Ashley 2011; Smith and Katz 2013). Due to their high-impact nature, reports of these events—including when and where they occurred—have been gathered and systematically archived for decades by organizations like the National Oceanic and Atmospheric Administration's Storm Prediction Center. Examples of how these data are used include storm warning verification (Brooks and Correia 2018), generating hazard climatologies (Brooks et al. 2003; Allen and Tippet 2015; Edwards et al. 2018), informing teleconnection relationships (Allen et al. 2015), exploring changes in the spatiotemporal occurrence of events (Brooks et al. 2014; Gensini and Brooks 2018), vulnerability and exposure analyses (Strader et al. 2017), and environmental analyses (Thompson et al. 2012). Of particular interest in the field of severe thunderstorm research has been the automated identification of convective storm mode (**CSM**) in weather radar data through manual (Smith et al. 2012; Ellis et al. 2019) or automated approaches (Haberlie and Ashley 2018; Gagne et al. 2019; McGovern et al. 2019; Jergensen et al. 2020).

Weather radar data has been used for decades to identify **CSM** (e.g., Fujita 1965). **CSM** identification can help assess the potential severity of an ongoing or imminent severe weather event (McNulty 1995; Smith et al. 2012), and can also be a useful tool for assessing operational (Snively and Gallus 2014) and climate model (Haberlie and Ashley 2019) performance. The maturation of historical weather radar data archives has allowed the climatological exploration of radar-derived event (e.g., thunderstorms, **CSM**) frequency (Matyas 2010; Fabry et al. 2017). For example, mean composite frequency of radar-derived events has been used to explore the relationship between locations with significant human-made land use modification and thunderstorm frequency (Ashley et al. 2012; Haberlie et al. 2015). Additionally, the millions of radar images generated and archived since the 1990s have been a great resource for applied machine learning researchers in the atmospheric and climate sciences (McGovern et al. 2019), including projects that train machine learning algorithms to identify **CSM** (e.g., Haberlie and Ashley 2018; Ashley et al. 2019; Jergensen et al. 2020). However, until now, there has been no attempt to create a curated dataset of radar images centred on classifiable "objects". These types of datasets are common in the field of machine learning, and are widely used for comparing the efficacy of different approaches. For example, the MNIST dataset (LeCun et al. 1998)—a collection of hand-written numbers—is publically available and has been referenced by tens of thousands of papers. Domain-specific examples include images of galaxies (Lintott et al. 2011) and satellite images centred on tropical systems (Knapp et al. 2016). This work is the first step in communicating the general attributes of this novel dataset which can inform future projects that use these data.

This work seeks to extend the methodology used by ”stationary window” radar analyses by instead centring the radar images to be composited on locations and times at which reported thunderstorm hazards occurred. This moving window approach has been used in previous work to assess the influence of multiple cities on thunderstorm activity (Fabry et al. 2017), generate composites of current and future heavy rainfall events (Prein et al. 2017), the successes and failures of machine learning model predictions (McGovern et al. 2019), and the strengths and weaknesses of various multi-model averaging approaches on modeled rainfall output (Clark et al. 2017). However, those works used 10s or 100s of "windows" and did not examine the spatial variability of the composites. This research expands these results to examine composites using over 500,000 radar images from various regions, times of the day, seasons, and event magnitudes. Additionally, it could provide a methodology for communicating morphological variability and evolution within events of interest beyond morphological statistics (Zick and Matyas 2016; Matyas et al. 2018). Through a moving window composite analysis, we visualize the spatiotemporal patterns in radar reflectivity in the vicinity of severe thunderstorm events in the conterminous United States (**CONUS**). Additionally, we show that the spatial, seasonal, and diurnal composite **CSM** tendencies match with those of existing **CSM** climatologies. This suggests that the dataset created through this work will be useful for machine learning applications, and in particular, **CSM** identification using image classification algorithms (LeCun et al. 1998).

2. Data and Methods

2.1 Radar data

This study utilizes historical (1996 – 2017) national reflectivity composite mosaic (2 x ~2 km grid spacing) data called NOWrad$_{tm}$ (The Weather Company). The raw data, which are integers (0 – 16) representing 5 dBZ bins from 0 – 80 dBZ, are sampled at 15-min intervals and interpolated to a 2 x 2 km (4 km^2) equal area grid that spans the CONUS in a rectangle from approximately 110 to 65 W and 25 to 50 N. These data have been used in a number of climatological studies (Fabry et al. 2017). Although issues exist within radar datasets, some of these are reduced in composite reflectivity by using data from multiple radars (Fabry et al. 2017). We address range- and terrain-based issues by limiting the study area to regions with good low-level radar coverage east of the Rocky Mountains (Figure 1). One important caveat is that dBZ was used in all calculations, and the values were not first converted to Z. Although the literature has argued for both approaches (Lakshmanan 2012; Warren and Protat 2019), these differences will not have a large influence on the interpretation of the results.

2.2 Severe Weather Event Data

The Storm Prediction Center's severe report dataset was used for event selection (SVRGIS; http://www.spc.noaa.gov/gis/svrgis). Although the dataset contains well-known biases (Allen and Tippett 2015; Edwards et al. 2018), no initial filtering is performed. All reports from 1996 – 2017 are cross-referenced with time-indexed radar reflectivity data to only select event reports that occurred within 7.5 minutes of available 15-minute radar data. An additional step subsets the data within the central and eastern CONUS where event locations are at least 256 km from the edge of the interpolated radar domain (Figure 1). After the filtering process is completed, over 90% of the original severe reports—24,940 tornado, 247,875 hail, and 275,568 wind—are retained. The large sample size, cross-referencing with radar data, and no temporal trend analyses limit the influence of the biases in the dataset. The starting coordinates (e.g., ‘slat’, ‘slon’) are used to determine the report’s location.

2.3 Selection of radar data using filtered SVRGIS reports

For all 548,383 filtered reports, radar data within a 256 by 256 pixel (~512 by ~512 km) box (herein, **report box**) around the report’s converted grid coordinate are extracted and saved (Figure 1.b-d). This distance was chosen to represent the mesoscale neighbourhood around each report since all **CSMs** exist within the meso-gamma to lower meso-alpha range (Markowski and Richardson 2010). To examine the accuracy of the process, bulk radar statistics within 64 km of the report’s grid location were calculated. Over 99% of the events had at least 40 km^2 (roughly the size of a convective cell; Miller and Mote 2017) of 40 dBZ or greater pixels in the buffer region. That is, almost all of the filtered reports were near legitimate (i.e., non-noise) dBZ values commonly associated with deep, moist convective precipitation rates (Parker and Knievel 2005). These images are used to generate composites.

2.4 Archetype generation

To examine the attributes of select **CSMs** (Gallus et al. 2008), an initial labelled dataset of 5,156 images was generated, consisting of: 1) Quasi-linear Convective System, or **QLCS** (n=2,330), 2) Cellular (n=2,453), and 3) Tropical (n = 373) examples. To create this dataset, images centred on the starting location of tornado reports from 1996 – 2017 were manually assigned to one of the aforementioned **CSMs**. Although the classifications are subjective, we followed the guidance of previous work (e.g., Gallus et al. 2008; Smith et al. 2012; Ashley et al. 2019; Ellis et al. 2019)—specifically, 1) QLCSs are identified by noting a linear organization of pixels ≥ 40 dBZ (i.e., at least a 3 to 1 length to width ratio) with a length of at least 100 km, 2) Cellular cases are identified by noting a circular organization to the ≥ 40 dBZ pixels in the vicinity of the report, and that contiguous circular region is entirely within a 100 x 100 km box around the report, and 3) Tropical cases are those that occurred near a HURDAT track (Landsea et al. 2015). The reports were gathered from the Southern United States (i.e., Oklahoma, Texas, Arkansas, Louisiana, Mississippi, Tennessee, Alabama, Florida, Georgia, South Carolina and North Carolina).

Probability matched mean (**PMM**) composites (Ebert 2001) are generated to visualize the tendency of reflectivity shape and intensity across the three **CSMs** and temporal periods (Figure 2). The probability matched approach is used over a simple mean because of the tendency for the latter approach to "smooth out" the large intensity gradients noted within precipitation rate products (Clark 2017)—one of which is reflectivity (dBZ). This approach produces more realistic spatial patterns of intensity while preserving the shape of the simple mean. Although this approach has historically been used to assess forecast skill of accumulated precipitation fields (Clark 2017) and simulated reflectivity factor (Surcel et al. 2014), recent work has used this method to generate representative examples of subsets using many observed radar images (McGovern et al. 2019; Lagerquist et al. 2020). To further illustrate the variability that is captured within the **PMM** composites, we first calculated the sums of the 25th and 75th percentile ranked intensity distributions within each subset. We then stratify these subsets by selecting only those images with a ranked intensity distribution sum less than or equal to (greater than or equal to) the 25th (75th) percentile distribution sums. In this way, we can visualize the extremes within the subsets, and communicate the morphological variability therein.

To confirm that the **PMM** composite images are more representative than less complex approaches, we compared them to composite images generated by a simple mean and median using the same radar image subsets. Specifically, we calculated the ranked reflectivity (dBZ) found within the composites (i.e., mean, median, and **PMM**) and compared those to the median ranked reflectivity for the entire subset (Figure 3). The simple mean composite image produces much broader areas of lower reflectivity values (i.e., < 15 dBZ) and fails to reproduce higher reflectivity values (i.e, > 15 dBZ) compared to any given image within the subset. The median composite image generally produces representative coverage for low reflectivity values, but, like the simple mean, it fails to reproduce higher reflectivity values. Ranked reflectivity from the **PMM** composite image, however, closely traces the median reflectivity ranks for all **CSMs**, suggesting it is representative of the intensity distribution one would see within the samples. This is consistent with previous work that demonstrated the advantages of **PMM** composites over the simple ensemble mean of precipitation accumulation, particularly for higher intensity values (Clark 2017).

The resulting **PMM** composites suggest that, for all of the selected tornado reports, the composite generated using affiliated 25th percentile radar images (Figure 2.a) resemble Cellular

CSM, whereas the composite of 75th percentile images (Figure 2.c) resemble QLCS **CSM**. The ranks for the first 0 dBZ pixel suggests that the median coverage of ≥ 5 dBZ pixels is around 36%, whereas this value is 47% for the 75th percentile distribution and 24% for the 25th percentile distribution (Figure 3.a). QLCS samples (Figure 2.d, e, f) tend to exhibit an elongated area of higher reflectivity values, and this pattern is consistent for the 25th and the 75th percentile composite images. The median coverage of non-zero pixels for QLCS images is around 42%, and the 25th and 75th percentile coverage are ~33% and ~52%, respectively (Figure 3.b). On the other hand, Cellular examples (Figure 2.g, h, i) show some variability between the 25th percentile images (Figure 2.g) and the 75th percentile images (Figure 2.i). Namely, there is a marked increase in coverage of non-zero reflectivity values for the 75th percentile images. This is the result of "cell-in-cluster" cases, which contrast the "isolated cellular" examples that comprise the 25th percentile subset. Median, 25th, and 75th percentile coverage of non-zero pixels are approximately 26%, 17%, and 37%, respectively, for Cellular examples (Figure 3.c). A noticeable and ubiquitous difference between the QLCS and Cellular composites is the lack of 30 dBZ and greater reflectivity values in the southern two-fifths of the Cellular composite images. This reflects the non-contiguous nature of "cell-in-cluster" **CSM** and the preference for tornado formation in "tail-end Charlies", or supercells that are on the southern flank of a storm cluster (Beveridge et al. 2019). Tropical examples (Figure 2.j, k, l) generally produce more widespread reflectivity values compared to Cellular, but have intensities lower than both QLCS and Cellular samples. Additionally, the westward offset of lower intensities for Tropical samples, particularly for the overall composite (Figure 2.k) and 75th percentile composite (Figure 2.l), matches up well with the preferred location of tornadoes relative to the centre of circulation for land falling storms in the CONUS (Edwards 2012). Median, 25th, and 75th percentile coverage of non-zero pixels for Tropical samples are approximately 50%, 39%, and 62%, respectively (Figure 3.d). Perhaps unsurprisingly, the QLCS/Cellular/Tropical composite depicted in Figure 2.b appears as a combination of the QLCS and Cellular composites (i.e., "mixed mode"), due to their abundance within the manually labelled data. It is also clear that Tropical samples generally have more non-zero pixels than QLCS and Cellular examples. However, median ≥ 40 dBZ coverage is greater for both QLCS (3.3%) and Cellular (2.2%), compared to Tropical (1.5%). These **PMM** composite archetypes and statistics are reasonable and can be used to qualitatively assess the **CSM** tendency within various subsets of unlabelled images.

3. Unlabelled image dataset

3.1 Composites from notable events

PMM composite images were generated for tornado reports during notable severe weather events (Figure 4). Specifically, we generated images for the: 1) 27 April 2011 tornado outbreak (Knupp et al. 2014); 2) 24-25 September 2005 Hurricane Rita tornadoes (Moore and Dixon 2011); 3) 4-5 April 2011 serial derecho event (Corfidi et al. 2016); and 4) 29 June 2012 progressive derecho event (Corfidi et al. 2016). The purpose of these analyses is to further communicate the utility of the composites, as well as identify the variability seen within even the same type of severe weather report. This also provides further verification that the approach is producing reasonable results by affording a qualitative comparison to the radar presentation during these well-documented events.

For the 27 April 2011 event, we focused on the early afternoon to evening period (1800 UTC to 0300 UTC). This period was chosen for demonstration purposes because the predominant storm mode for tornado producing storms was cellular (Knupp et al. 2014), and this tendency is clearly illustrated in Figure 4.a, b, c. Specifically, the pattern shows a strong, high intensity (> 50 dBZ), "kidney-bean-shaped" region within 25 km of the center of the image (i.e., the location of the storm reports) in the overall **PMM** composite (Figure 4.b), as well as the 25^{th} (Figure 4.a) and 75^{th} percentile (Figure 4.c) composites. Additionally, the northern half of the composite has greater coverage of high-intensity pixels, which matches the regional radar depiction during this event. The variability between the 25^{th} and 75^{th} percentile images denote the "isolated cellular" and "cell-in-cluster" events that occurred during this event, and the overall composite reflects these tendencies. Similarly, the composite from the Rita event—where reports were selected from 1400 UTC on 24 September 2005 to 0000 UTC on 26 September 2005—depicts a "bulls-eye" in the center of the image, but with a contrasting northward (Figure 4.d) and westward preference (Figure 4.e, f) of higher pixel coverage. This pattern represents the preferred location of tornado reports relative to the center of Rita (Edwards 2012) and the evolution of this location during the event. Initially, tornadoes were observed in the upper right quadrant of the storm, but this region shifted to the lower right quadrant later in the period. For the wind-report examples, the squall line that produced a serial derecho (Corfidi et al. 2016) is clearly resolved within the 25th percentile (Figure 4.g), overall (Figure 4.h) and 75th percentile (Figure 4.i) composites that include images from 1300 UTC on 4 April 2011 to 0300 UTC on 5 April 2011. Only the central part of the images depicts the classic "quasi-linear" region of high-intensity pixels associated with intense squall lines due to the shifting orientation of the squall line across its ~1000 km axis. Similarly, the progressive derecho event of 29 June 2012 (Figure 4.j, k, l) captures the comparatively more compact linear structure and trailing-stratiform precipitation that is typical of the leading-line / trailing-stratiform pattern (Parker and Johnson 2000). Similar to the Rita event, the stratification by percentile appears to capture the initial cellular structure across the Midwest and the leading-line / trailing-stratiform structure as it moved to the east coast later in its life cycle. Again, Figure 5 illustrates that the **PMM** approach is more representative of the reflectivity distribution than the mean or median composite images for these events. The April 27th 2011 event (Figure 5.a) and the June 2012 derecho both have lower median coverage of non-zero pixels compared to the Rita event (Figure 5.b) and the progressive derecho event (Figure 5.c). Although there is variability in the orientation, intensity, and location of **CSM** structures relative to storm reports, tendencies in reflectivity patterns are captured by the composites.

3.2 Composites stratified by tornado damage rating

Previous work has shown a strong relationship between **CSM** and EF-scale rating (Trapp et al. 2005; Smith et al. 2012; Ashley et al. 2019). Namely, a Cellular **CSM** is most commonly associated with significant (≥ EF2) to violent (≥ EF4) tornadoes. Thus, composites stratified by EF-scale rating should reflect these findings. For all tornado events considered in this study that were given a rating (n=24,850), their associated images were stratified into groups ranging from EF0 to EF5 (Figure 6; Figure 7). Indeed, the **PMM** composites show a steady transition from "mixed mode" QLCS and Cellular **CSM** archetypes (Figure 2) for EF0 to EF2 (Figure 6) to cellular for EF3 and EF4 (Figure 7.a-f) to isolated cellular for EF5 (Figure 7.g-i). Although there is variability within these composites, there is a clear trend of a reduction in reflectivity coverage consistent with a shift from QLCS to Cellular **CSM** as EF-scale rating increases (Figure 8). There is also a marked reduction in the coverage of non-zero pixels in the "maximum" ranked distribution as rating increases. More modest reductions within increasing EF-scale rating are evident in the median, 25^{th}, and 75^{th} percentile non-zero pixel coverage, with coverage maximizing at EF1 (32%, 21%, and 45%, respectively), and minimizing for EF5s (18%, 12%, and 31%, respectively). Interestingly, however, even the EF3 and EF4 composites have areas of mean convective (≥ 40 dBZ) reflectivity extending to the north, which suggests the possibility of more specific **CSMs** like those proposed by Smith et al. (2012), namely, cell-in-line and cell-in-cluster, in addition to QLCS. This "mixed-mode" is illustrated by the differences between the 25^{th} (Figure 6.a, d, g; Figure 7.a, d) and 75^{th} (Figure 6.c, f, i; Figure 7.c, f) percentile **PMM** composite images—specifically, the Cellular **CSM** in the 25^{th} percentile images and the QLCS / clustered **CSM** in the 75^{th} percentile images. The **CSMs** depicted in the 75^{th} percentile images are associated with problematic issues like the highest fatality and injury rate per tornado (supercell in line; Brotzge et al. 2013) and lowest probability of detection (QLCS; Brotzge et al. 2013). These results affirm that even significant to violent tornadoes can occur in “messy” or mixed-mode mesoscale convective scenarios, leading to reductions in warning efficacy.

3.3 Spatiotemporal variability of composites

To facilitate spatial analyses and comparisons, the eastern CONUS is organized into twenty-nine 512 x 512 km grids and one ocean control grid (Figure 9). Storm reports are associated with a grid using a one-to-one spatial join in *ArcGIS Pro*. Next, **PMM** composites are generated for each grid by only using images associated with reports that occur within that grid (Figure 9). For example, the image plotted within grid 22 (Birmingham) in Figure 9.a is the **PMM** composite for all images associated with any severe (tornado, hail, and wind) report that occurred within that grid cell. All of the **PMM** composite images have the same scale as the original data. That is, the **PMM** composite is inserted onto the 2-km equal area grid by anchoring the centre of the image on the pixel closest to the centroid of each grid, and filling out 128 pixels to the north, south, east and west of that central pixel. Through this analysis, we can assess the spatial variability in “typical” radar reflectivity appearance. The colour map used in the composite figures was chosen to replicate the typical colour scale used when presenting weather radar reflectivity. The authors feel that the disadvantages of the generally poor colour map choice are balanced by the familiarity experts and non-experts have with this colour scale.

Marked spatial patterns are illustrated by stratifying the data into gridded regions. The composites for all events (Figure 9.a), as well as those stratified by hazard type (Figure 9.b-d), show a tendency for radar images to exhibit a more cellular appearance in the High Plains with an increasingly QLCS-like appearance in Southeast CONUS. This pattern is particularly evident within the tornado composites (Figure 9.b). Southern Great Plains tornado grids (e.g., 14-Wichita and 20-Dallas) match up well with the cellular archetype depicted in Figure 2.g-i, whereas tornado grids within the Southeast CONUS (e.g., 21-Little Rock and 22-Birmingham) match with the QLCS archetype (Figure 2.d-f). Conversely, hail composites (Figure 9.c) suggest that the preferred storm mode is predominately cellular. Although, the cells appear to be more isolated in grids like 13-Denver compared to 16-Nashville. Wind composites (Figure 9.d) show a QLCS-like pattern in the Southeast CONUS, and a "mixed mode" pattern as depicted in Figure 2.b in the Midwest CONUS. The lack of ≥ 5 dBZ to the NW and SE of severe thunderstorm reports is expected and ubiquitous throughout the composites. The initiation and sustenance of deep, moist convection that produces severe weather requires a lifting mechanism, which is typically provided by frontal boundaries (McNulty 1995). To the NW of the report, this is often an area where cold or dry air has undercut warm or moist air, and instability has decreased. To the SE of the report, this area often experiences a capping inversion and air parcels are spatially displaced from an adequate lifting mechanism.

Extending the analysis to warm (April – September) and cool (October – March) seasons reveals temporal variability within the grids (Figure 10). In general, the spatial coverage of the "mean storm" either increases or becomes more elongated during the cool season, particularly for tornado and wind events. Summer tornado events produce composites most similar to the cellular archetype (Figure 2.g-i) in the Great Plains and Midwest CONUS, and an increasing QLCS-like pattern as one moves into the Southeast CONUS (Figure 10.a). Focusing on the eastward transition between grids 19-Amarillo, 20-Dallas, 21-Little Rock, and 22-Birmingham, there is a clear evolution from cellular to QLCS-like composites. In contrast, the eastward transition from 7-Casper, 8-Sioux Falls, 9-Des Moines, and 10-Chicago shows a more subtle cellular to QLCS-like transition, potentially caused by more compact QLCSs or a more balanced mix of Cellular and QLCS structures compared to the Southeast. Perhaps not surprisingly, 27-Baton Rouge, 28-Mobile, and 29-Orlando, exhibit a Tropical-like structure in their warm-season tornado composites. These **CSMs** shift towards QLCS-like structures in the cool season (Figure 10.b), and this change is ubiquitous across the grids. This shift is not as obvious for hail events (Figure 10.c-d), and although a clear elongation of the spatial coverage of reflectivity intensity is noted, the best qualitative fit for the grids would still be the cellular archetype in Figure 2.g-i. Similar to the tornado composites, the composites for wind events shift from a cellular or mixed-mode pattern in the warm season to a QLCS pattern in the cool season (Figure 10.e-f). The seasonal dichotomy could be explained by a balance between instability and convective inhibition. Convective ($\geq$ 40 dBZ) reflectivity values are often associated with vigorous deep, moist convection (Ashley et al. 2012), and environmental conditions that support such convection have favorable thermodynamics and kinematics (McNulty 1995). However, the utilization of these ingredients by potential storms is conditioned on other factors such as the strength of a capping inversion and forcing for ascent. During the spring and early summer, a large portion of the study area experiences supportive thermodynamics, kinematics, and conditional environmental factors that lead to the frequent development of widespread convection (Doswell 2001; Gensini and Ashley 2011). Moving into the late summer and early fall, stronger capping inversions and weaker forcing can limit the coverage of convection. The result within the composites is the contraction of the “mean storms” due to the limited coverage of non-zero reflectivity values as a response to increasingly localized and less widespread supportive environments during this period.

We stratified the reports into two subsets to examine the influence time of day had on the composites, namely: 1) an early afternoon and early evening subset (1700 – 0500 UTC); and 2) a night and morning subset (0500 – 1700 UTC). The limitations of choosing these subsets is that the amount of daylight hours, as well as local noon and local midnight, differs over the course of a year and within the study area. Thus, these periods should be considered only roughly representative of the typical time periods in which initial convection develops (early afternoon and evening) and when upscale growth has occurred (night and morning) based on previous work (Carbone and Tuttle 2008). Similar patterns to the seasonal analyses emerge from the diurnally-stratified composites (Figure 11). In particular, the transition from the afternoon and evening subset to the night and morning subset results in an increased area covered by the 5 dBZ contour for all of the hazard types and most of the grids. Tornado composites (Figure 11.a-b) exhibit a marked expansion in spatial coverage during the night and morning period, including higher intensity contours that denote regions of convection (i.e., 40 dBZ). Some of the more dramatic diurnal increases in reflectivity coverage includes 9-Des Moines and 15-St. Louis. Hail events (Figure 11.c-d) experience an expansion in spatial coverage and a change in how the most intense reflectivities are oriented relative to the areas of weaker mean reflectivity during the night and morning period. Specifically, areas of higher intensity are on the southern flank of the 5 dBZ contour region, whereas the afternoon to evening composites have this area on the southwest flank, and this pattern is particularly evident in grids 9-Des Moines and 10-Chicago. Based on when hail typically occurs in this area (i.e., late spring and early summer), it is possible that this signal is related to the nocturnal low level jet interacting with frontal boundaries (Walters et al. 2008). Wind composites similarly show an expansion of weaker reflectivity (≥ 5 dBZ) and convective reflectivity (≥ 40 dBZ) for many of the grids in the night and morning subsets (Figure 11.e-f). This strong signal suggests a preference for QLCS-like structures over cellular structures during this time of the day. Although peak heating occurs during the afternoon, the upscale growth of organized convection associated with severe thunderstorm events is largely relegated to the overnight hours, particularly during the summer (Carbone and Tuttle 2008; Geerts et al. 2017). The merging and subsequent reinforcement of cold pools as an event matures results in the mesoscale area favorable for lifting parcels to the level of free convection to increase from the meso-gamma scale (~10 km) to the meso-beta scale (~100 km; Coniglio et al. 2010). Additionally, supportive thermodynamics and kinematics that develop exclusively during the overnight hours allows the development of convection that is displaced from surface frontal boundaries (Walters et al. 2008; Weckworth et al. 2019). The overall effect of these factors results in the increase in coverage of convection during the overnight and morning period.

4. Discussion and Conclusions

This study used a moving window composite analysis to illustrate the climatological tendency of radar-derived spatial patterns affiliated with recorded severe thunderstorm hazards in the eastern two-thirds of the CONUS. Three convective storm modes (**CSMs**) were chosen to illustrate the variability between composites generated for approximately 5,000 manually identified QLCS, Cellular, and Tropical samples. For unlabelled tornado samples, the images were first stratified by F/EF scale to examine the **CSM** tendency within the resulting composites. To examine the spatiotemporal variability of the composites, over 500,000 images were used to create composites for 30 “report box” grids over the eastern CONUS. This analysis informed an exploration of not only the regional variability of these composites, but also the seasonal and diurnal variability therein.

The results affirm previous work that examined **CSM** within the CONUS (Smith et al. 2012; Ashley et al. 2019). In particular, strong tornadoes were associated with a “Cellular” **CSM** tendency, whereas weaker tornadoes were associated with “QLCS” or mixed Cellular/QLCS **CSM** tendency. **CSM** tendency within Great Plains grids was Cellular, whereas the tendency for Southeast CONUS grids was QLCS or mixed Cellular/QLCS. Day and warm-season events preferred a Cellular **CSM**, whereas cool-season and night events preferred QLCS or mixed Cellular/QLCS. The results show the utility of the moving window composite approach, due to its agreement with existing manual and automated studies of spatiotemporal **CSM** variability.

Future work using these data should explore ways of using semi-supervised (Zhu and Goldberg 2009) machine learning classification techniques to assign **CSM** labels to the 500,000 extracted images. A large dataset of labelled images would be useful to the meteorology and climate research community, particularly those who are engaged in image classification applications. For example, these data can populate an "image search engine" that can perform image retrieval tasks (Guo et al. 2016). Users of the image search engine would then be able to query the severe weather report dataset by the appearance of the radar image, in addition to the attributes provided within SVRGIS (time, location, magnitude, etc.). Such projects have been successful in other domains (LeCun et al. 1998; Lintott et al. 2011; Knapp et al. 2016) by: 1) providing a consistent dataset from which to draw examples; and 2) adding context to the performance of new machine learning approaches. Additionally, these and similar projects have improved public access to scientific datasets, educated non-experts on physical phenomena, and even included so-called "citizen scientists" in the dataset-building process. Like other projects, this dataset can be modular and add new data as it becomes available through a versioning process.

Acknowledgements: This work is supported in part by Louisiana Board of Regents RCS Grant LEQSF(2019-22)-RD-A-07, National Science Foundation Grant ATM-1637225,and NOAA grant NA13OAR4310183. We would like to thank Ryan Lagerquist for the probability matched mean code that helped create the composites. Sample analyses and instructions on how to access the data used in this work are available at https://github.com/ahaberlie/SVRIMG.

Works Cited:

Allen, J. T., and Tippett, M. K. (2015). The characteristics of United States hail reports: 1955-2014. *E-Journal of Severe Storms Meteorology*, 10(3).

Allen, J. T., Tippett, M. K., and Sobel, A. H. (2015). Influence of the El Niño/Southern Oscillation on tornado and hail frequency in the United States. *Nature Geoscience,* 8, 278.

Ashley, W. S. (2007). Spatial and temporal analysis of tornado fatalities in the United States: 1880-2005. *Weather and Forecasting*, 22, 1214-1228.

Ashley, W. S., Bentley, M. L., and Stallins, J. A. (2012) Urban-induced thunderstorm modification in the Southeast United States. *Climatic Change,* 113, 481-498.

Ashley, W. S., Haberlie, A. M., and Strohm, J. (2019). A climatology of quasi-linear convective systems and their hazards in the United States. *Weather and Forecasting*, 34, 1605-1631.

Beveridge, S. L., Houser, J. L., and Marzola, S. R. (2019) A Statistical Evaluation of Tornado-Production Tendencies of Southernmost Supercells Compared to Adjacent Supercells in a North–South-Oriented Line. *E-Journal of Severe Storms Meteorology,* 14,

Black, A. W., and Ashley W. S. (2010). Nontornadic convective wind fatalities in the United States. *Natural Hazards,* 54, 355-366.

Brooks, H. E., Doswell III, C. A, and Kay, M. P. (2003). Climatological estimates of local daily tornado probability for the United States. *Weather and Forecasting,* 18, 626-640.

Brooks, H. E., Carbin, G. W., and Marsh, P. T. (2014). Increased variability of tornado occurrence in the United States. *Science,* 346, 349-352.

Brooks, H. E., and Correia Jr., J. (2018). Long-term performance metrics for National Weather Service tornado warnings. *Weather and Forecasting* 33, 1501-1511.

Brotzge, J. A., Nelson, S. E., Thompson, R. L., and Smith, B. T. (2013). Tornado probability of detection and lead time as a function of convective mode and environmental parameters. *Weather and Forecasting*, 28, 1261-1276.

Carbone, R. E., and Tuttle, J.D. (2008). Rainfall occurrence in the US warm season: The diurnal cycle. *Journal of Climate*, 21, 4132-4146.

Clark, A. J. (2017). Generation of ensemble mean precipitation forecasts from convection-allowing ensembles. *Weather and Forecasting*, **32**, 1569-1583.

Coniglio, M. C., Hwang, J. Y., and Stensrud, D. J. (2010). Environmental factors in the upscale growth and longevity of MCSs derived from Rapid Update Cycle analyses. *Monthly Weather Review*, 138, 3514-3539.

Corfidi, S. F., Coniglio, M. C., Cohen, A. E., and Mead, C. M. (2016). A proposed revision to the definition of “derecho”. *Bulletin of the American Meteorological Society*, 97, 935-949.

Doswell, C.A., (2001). Severe convective storms—An overview. In Severe convective storms (pp. 1-26). *American Meteorological Society*, Boston, MA.

Ebert, E. E. 2001. Ability of a poor man's ensemble to predict the probability and distribution of precipitation. *Monthly Weather Review*, 129, 2461-2480.

Edwards, R. (2012). Tropical cyclone tornadoes: A review of knowledge in research and prediction. *E-Journal of Severe Storms Meteorology*, 7, 6.

Edwards, R., Allen, J. T., and Carbin, G. W. (2018). Reliability and climatological impacts of convective wind estimations. *Journal of Applied Meteorology and Climatology*, 57, 1825-1845.

Ellis, K. N., Burow D., Gassert, K. N., Mason, L. R., and Porter., M.S. (2019). Forecaster Perceptions and Climatological Analysis of the Influence of Convective Mode on Tornado Climatology and Warning Success. *Annals of the American Association of Geographers*, 2019 1-20.

Fabry, F., Meunier, V., Treserras, B. P., Cournoyer, A., and Nelson, B. (2017). On the climatological use of radar data mosaics: Possibilities and challenges. *Bulletin of the American Meteorological Society*, 98, 2135-2148.

Fujita, T. T., (1965). Formation and steering mechanisms of tornado cyclones and associated hook echoes. *Monthly Weather Review*, 93, 67-78.

Gagne II, D.J., Haupt, S. E., Nychka, D. W., and Thompson, G. (2019). Interpretable deep learning for spatial analysis of severe hailstorms. *Monthly Weather Review*, 147, 2827-2845.

Gallus Jr, W. A., Snook, N. A., and Johnson, E. V. (2008). Spring and summer severe weather reports over the Midwest as a function of convective mode: A preliminary study. *Weather and Forecasting*, 23, 101-113.

Geerts, B., and coauthors. (2017). The 2015 plains elevated convection at night field project. *Bulletin of the American Meteorological Society*, 98, 767-786.

Gensini, V.A. and Ashley, W.S., (2011). Climatology of potentially severe convective environments from the North American Regional Reanalysis. *E-Journal of Severe Storms Meteorology*, 6(8).

Gensini, V. A., and Brooks, H. E. (2018). Spatial trends in United States tornado frequency. *npj Climate and Atmospheric Science*, 1, 38.

Guo, Y., Liu, Y., Oerlemans, A., Lao, S., Wu, S., and Lew, M. S. (2016). Deep learning for visual understanding: A review. Neurocomputing, 187, 27-48.

Haberlie, A., Ashley, W. S., and Pingel, T. (2015). The effect of urbanization on the climatology of thunderstorm initiation. *Quarterly Journal of the Royal Meteorological Society*, 141, 663-675.

Haberlie, A. M., and Ashley, W. S. (2018). Identifying mesoscale convective systems in radar mosaics. Part I. Segmentation and classification. *Journal of Applied Meteorology and Climatology*, 57, 1575-1598

Haberlie, A. M., and Ashley, W. S. (2019). Climatological representation of mesoscale convective systems in a dynamically downscaled climate simulation. *International Journal of Climatology*, 39, 1144-1153.

Jergensen, G. E., McGovern, A., Lagerquist, R., and Smith, T. (2020). Classifying convective storms using machine learning. *Weather and Forecasting*. In Press.

Knapp, K. R., Matthews, J. L., Kossin, J. P., and Hennon, C. C. (2016) Identification of tropical cyclone storm types using crowdsourcing. *Monthly Weather Review*, 144, 3783-3798.

Knupp, K. R., and coauthors. (2014). Meteorological overview of the devastating 27 April 2011 tornado outbreak. *Bulletin of the American Meteorological Society*, 95, 1041-1062.

Landsea, C., J. Franklin, and J. Beven. (2015). The revised Atlantic hurricane database (HURDAT2). NOAA/NHC.[Available online at nhc. noaa. gov.]

LeCun, Y., Bottou, L., Bengio, Y., and Haffner, P. (1998). Gradient-based learning applied to document recognition. *Proceedings of the IEEE*, 86, 2278-2324.

Lintott, C., and coauthors. (2011). Galaxy Zoo 1: data release of morphological classifications for nearly 900 000 galaxies. *Monthly Notices of the Royal Astronomical Society*, 410, 166-178.

Matyas, C. J. (2010). Use of ground-based radar for climate- scale studies of weather and rainfall. *Geography Compass*, 4, 1218-1237.

Matyas, C. J., Zick, S. E., and Tang, J. (2018). Using an object-based approach to quantify the spatial structure of reflectivity regions in hurricane Isabel (2003). Part I: comparisons between radar observations and model simulations. *Monthly Weather Review*, 146, 1319-1340.

Markowski, P., and Richardson, Y. (2011): *Mesoscale Meteorology in Midlatitudes*. Wiley-Blackwell, 424 pp.

McGovern, A., Lagerquist, R., Gagne, D. J., Jergensen, G. E., Elmore, K. L., Homeyer, C.R., and Smith, T. (2019). Making the black box more transparent: Understanding the physical implications of machine learning. *Bulletin of the American Meteorological Society*, 100, 2175-2199.

McNulty, R.P., 1995. Severe and convective weather: A central region forecasting challenge. *Weather and Forecasting*, 10, 187-202.

Miller, P. W., and Mote, T. L. (2017). Standardizing the definition of a ''pulse'' thunderstorm. *Bulletin of the American Meteorological Society*, 98, 905–913.

Moore, T. W., and Dixon, R. W. (2011). Climatology of tornadoes associated with Gulf Coast-landfalling hurricanes. *Geographical Review*, 101, 371-395.

Parker, M. D., and Johnson, R. H. (2000). Organizational modes of midlatitude mesoscale convective systems. Monthly Weather Review, 128, 3413-3436.

Parker, M. D., and Knievel, J. C. (2005). Do meteorologists suppress thunderstorms?: Radar-derived statistics and the behavior of moist convection. *Bulletin of the American Meteorological Society*, 86, 341–358.

Prein, A. F., Liu, C., Ikeda, K., Bullock, R., Rasmussen, R. M., Holland, G. J., and Clark, M. (2017). Simulating North American mesoscale convective systems with a convection-permitting climate model. Climate Dynamics, 2017, 1-16.

Schoen, J., and Ashley, W. S. (2011). A climatology of fatal convective wind events by storm type. *Weather and Forecasting*, 26, 109-121.

Smith, B. T., Thompson, R. L., Grams, J. S., Broyles, C., and Brooks, H. E. (2012). Convective modes for significant severe thunderstorms in the contiguous United States. Part I: Storm classification and climatology. *Weather and Forecasting*, 27, 1114-1135.

Smith, A. B., and Katz, R. W. (2013). US billion-dollar weather and climate disasters: data sources, trends, accuracy and biases. *Natural Hazards*, 67, 387-410.

Snively, D. V., and Gallus Jr., W. A. (2014). Prediction of convective morphology in near-cloud-permitting WRF model simulations. *Weather and Forecasting*, 29, 130-149.

Strader, S. M., Ashley, W. S., Pingel, T. J., and Krmenec, A. J. (2017). Observed and projected changes in United States tornado exposure. *Weather, Climate, and Society*, 9, 109-123.

Surcel, M., Zawadzki, I., and Yau, M. K. (2014). On the filtering properties of ensemble averaging for storm-scale precipitation forecasts. *Monthly Weather Review*, 142, 1093-1105.

Thompson, R. L., Smith, B. T., Grams, J. S., Dean, A. R., and Broyles, C. (2012). Convective modes for significant severe thunderstorms in the contiguous United States. Part II: Supercell and QLCS tornado environments. *Weather and Forecasting*, 27, 1136-1154.

Trapp, R. J., Tessendorf, S. A., Godfrey, E. S., and Brooks, H. E. (2005). Tornadoes from squall lines and bow echoes. Part I: Climatological distribution. *Weather and Forecasting*, 20, 23–34.

Walters, C. K., Winkler, J. A., Shadbolt, R. P., van Ravensway, J., and Bierly, G. D. 2008. A long-term climatology of southerly and northerly low-level jets for the central United States. *Annals of the Association of American Geographers*, 98, 521-552.

Weckwerth, T. M., Hanesiak, J., Wilson, J. W., Trier, S.B., Degelia, S. K., Gallus Jr, W. A., Roberts, R. D., and Wang, X. (2019). Nocturnal convection initiation during PECAN 2015. *Bulletin of the American Meteorological Society*, 100, 2223-2239.

Zick, S. E., and Matyas, C. J. (2016). A shape metric methodology for studying the evolving geometries of synoptic-scale precipitation patterns in tropical cyclones. *Annals of the American Association of Geographers*, 106, 1217-1235.

Zhu, X., and Goldberg, A. B. (2009). Synthesis Lectures on Artificial Intelligence and Machine Learning: Introduction to semi-supervised learning: , Morgan and Claypool Publishers, Williston, VT.

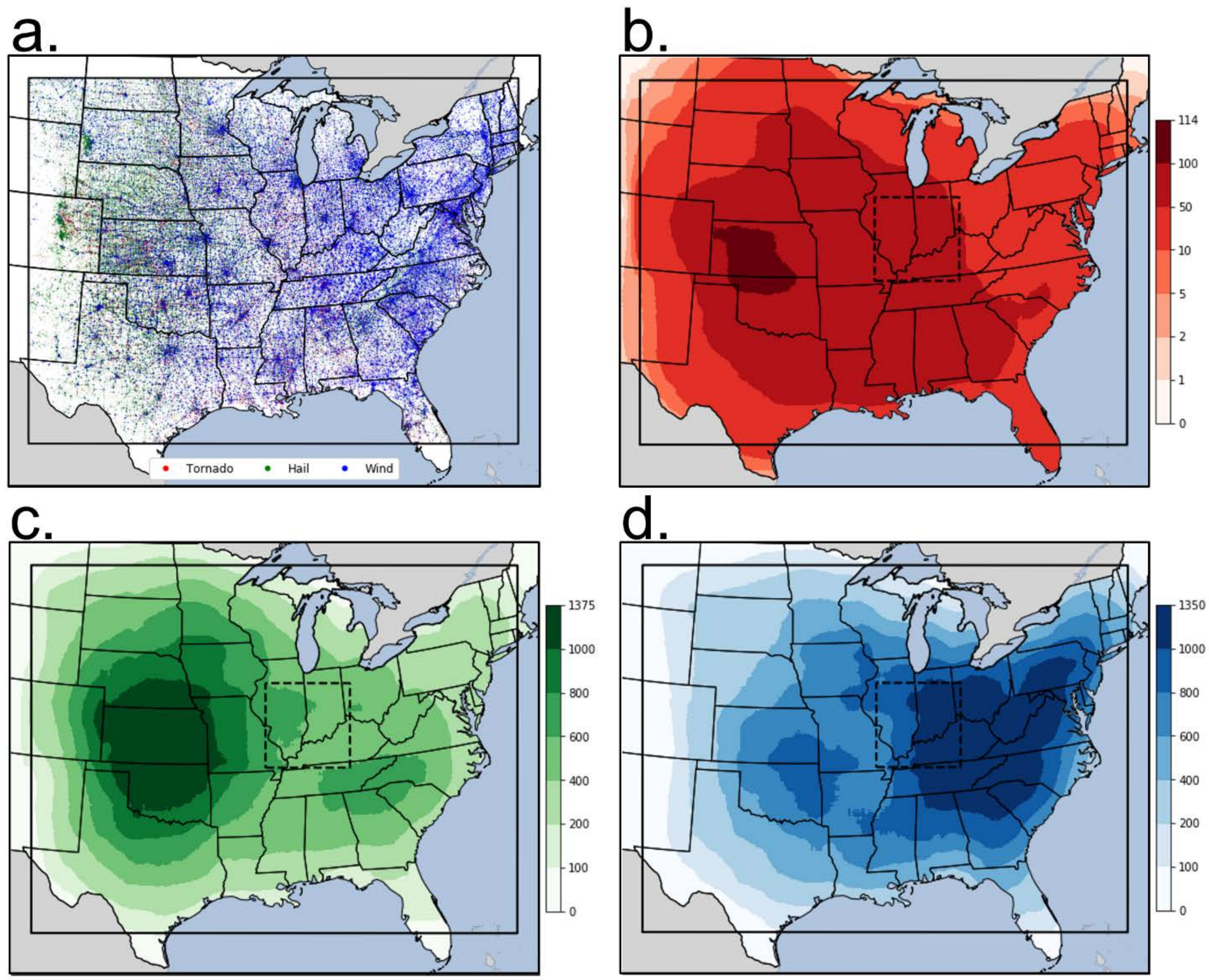

Figure 1. Study domain (black outline) and data from 1996 – 2017 for (a) severe weather report locations, and annual mean “report box” frequencies for (b) tornadoes, (c) hail, and (d) wind. The black dashed box in (b-d) represents an example of the extent of a 512 x 512 km “report box”.

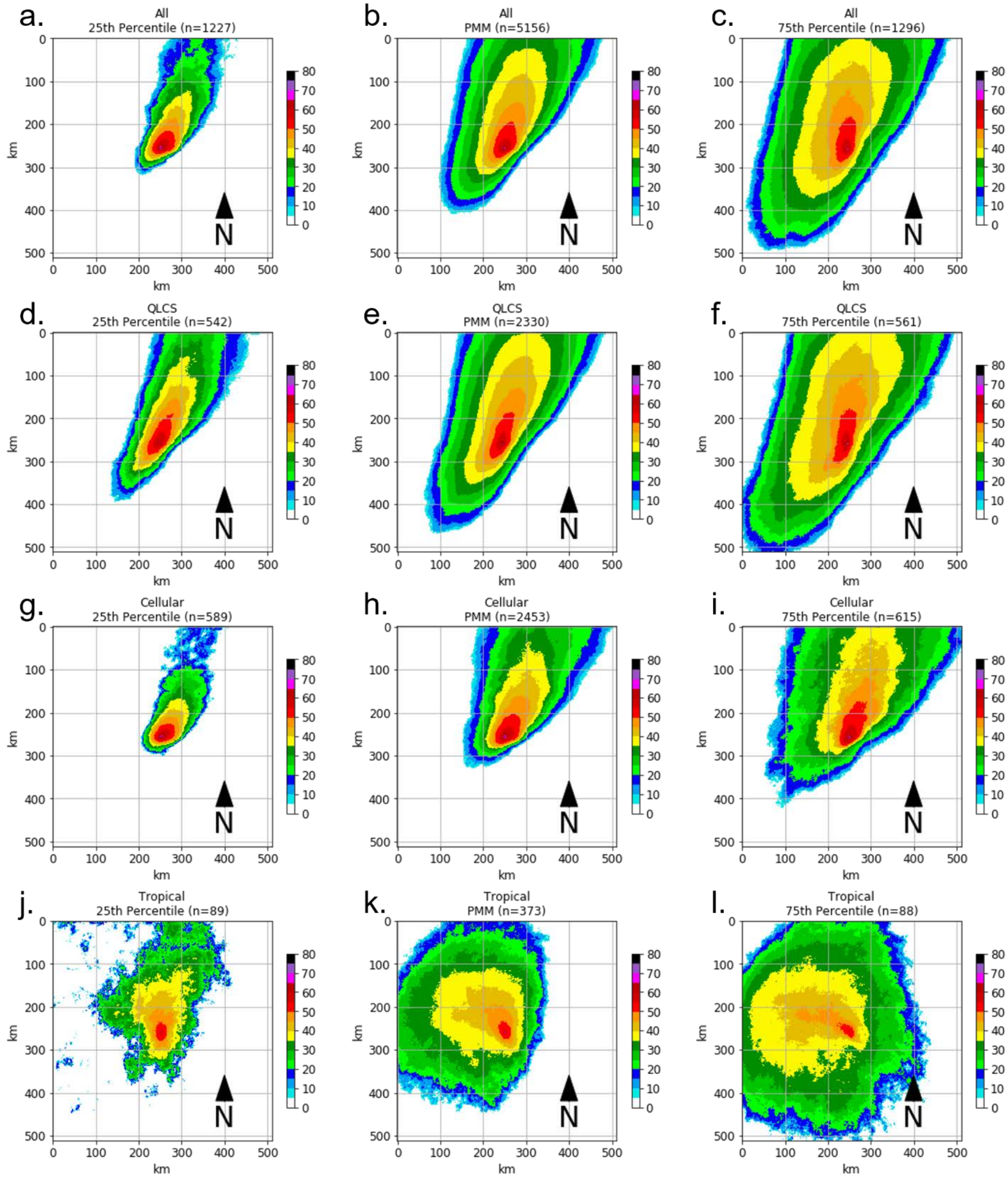
a.
All
25th Percentile (n=1227)
b.
All
PMM (n=5156)
c.
All
75th Percentile (n=1296)
d.
QLCS
25th Percentile (n=542)
e.
QLCS
PMM (n=2330)
f.
QLCS
75th Percentile (n=561)
g.
Cellular
25th Percentile (n=589)
h.
Cellular
PMM (n=2453)
i.
Cellular
75th Percentile (n=615)
j.
Tropical
25th Percentile (n=89)
k.
Tropical
PMM (n=373)
l.
Tropical
75th Percentile (n=88)
km
N

Figure 2. Probability matched mean composites calculated using subsets of reflectivity images centred on manually identified tornado (≥ EF1) reports from 1996 – 2017 in the Southeast U.S organized by convective storm mode. The convective storm modes depicted are (a, b, c) QLCS, Cellular, and Tropical, (d, e, f) QLCS, (g, h, i) Cellular, and (j, k, l) Tropical. Three probability matched mean composites were generated from each convective storm mode subset, namely: (a, d, g, j) only images with distribution sums ≤ 25th percentile distribution sum, (b, e, h, k) all images, and (c, f, i, l) only images with distribution sums ≥ 75th percentile distribution sum.

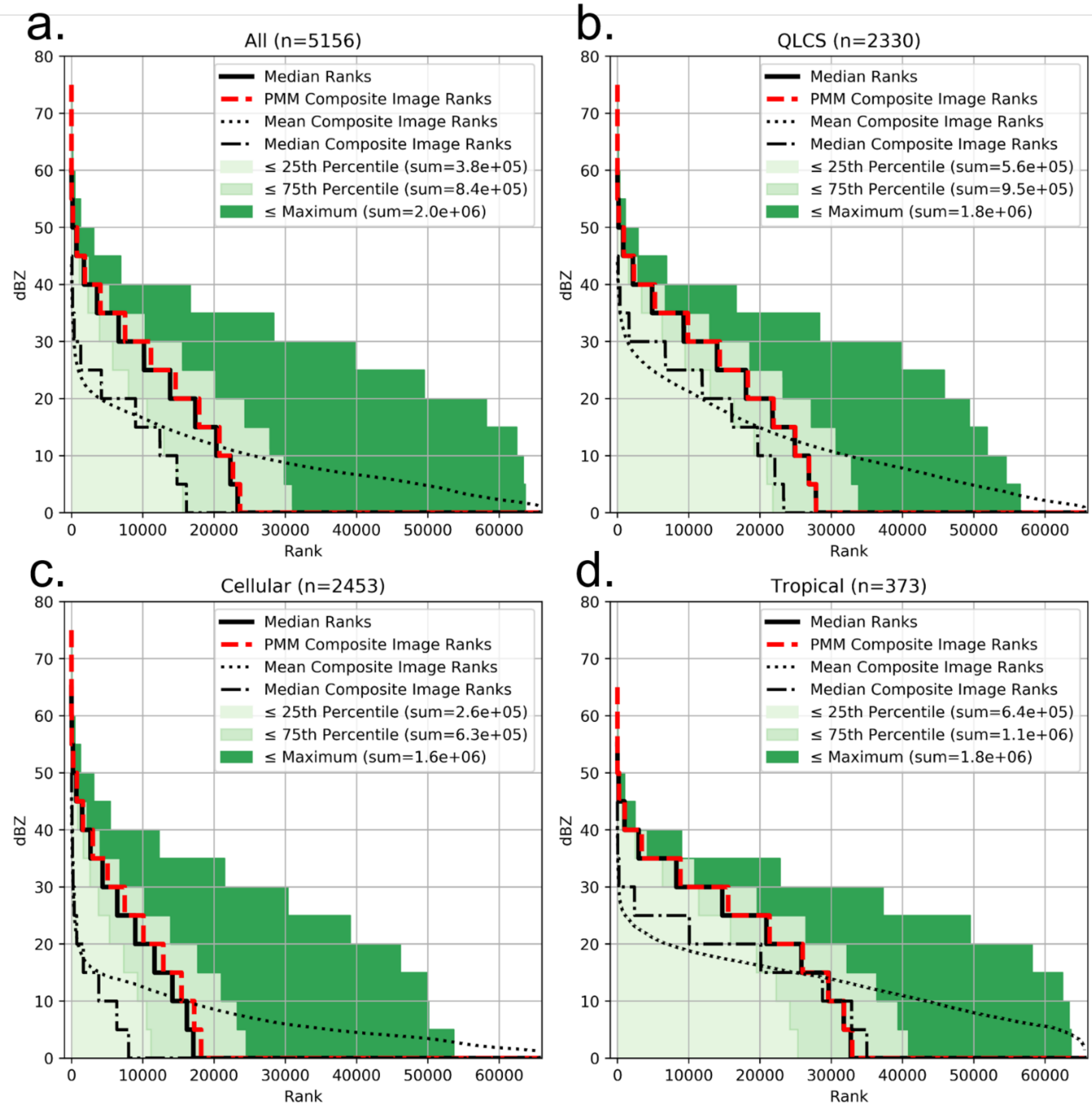

Figure 3. Median ranked intensity (black line) in units of dBZ for all images within each convective storm mode subset, namely (a) QLCS, Cellular, and Tropical, (b) QLCS, (c) Cellular, and (d) Tropical. For each subset, ranked intensity is also plotted for composite images generated using a probability matched mean (red dashed line), simple mean (black dotted line), and median (black dash-dotted line). The regions representing the ≤ 25th percentile

(lightest green), 25th to 75th percentile (medium green), and 75th to maximum (darkest green) distribution regions are colour filled.

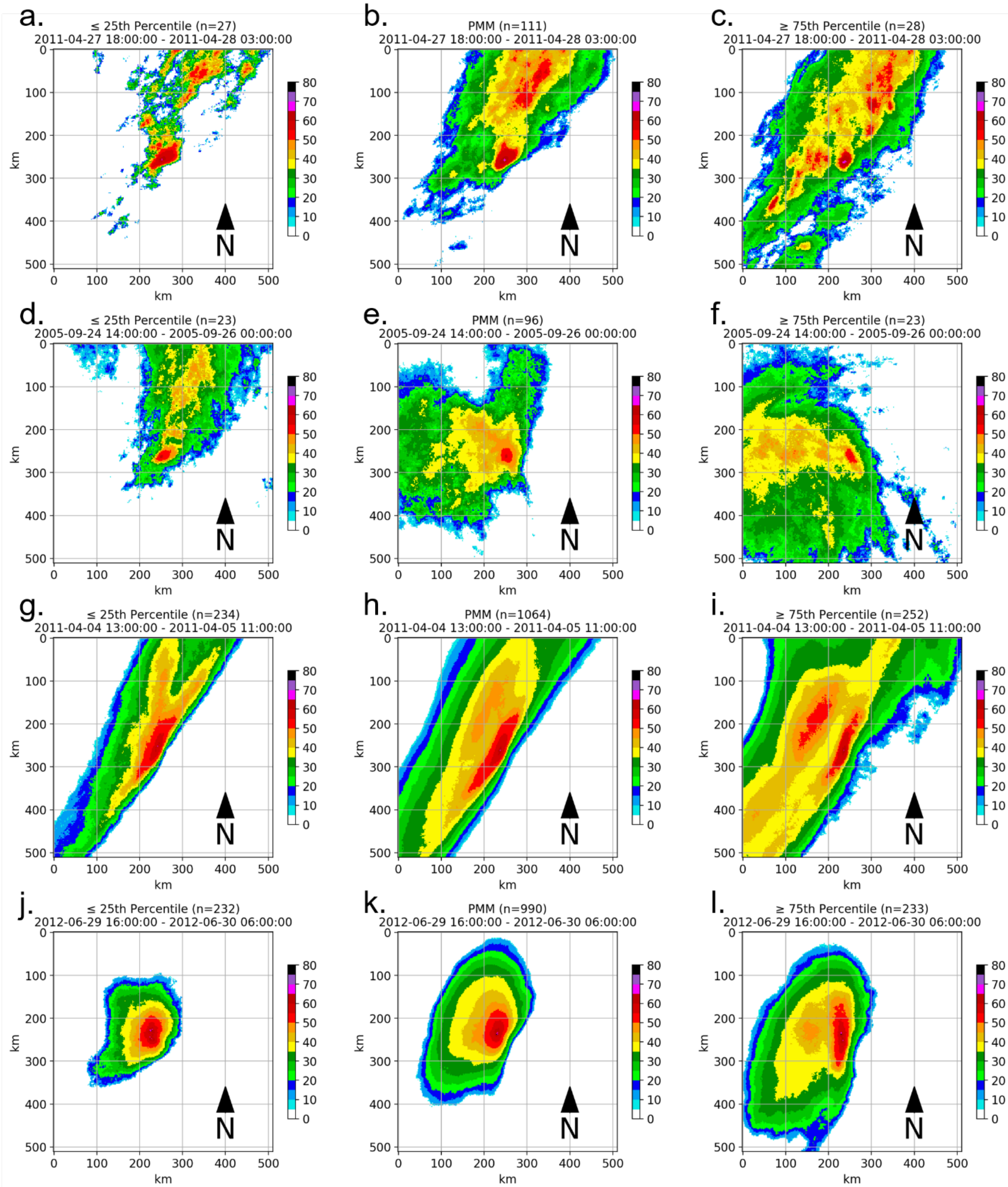
a.
≤ 25th Percentile (n=27)
2011-04-27 18:00:00 - 2011-04-28 03:00:00
b.
PMM (n=111)
2011-04-27 18:00:00 - 2011-04-28 03:00:00
c.
≥ 75th Percentile (n=28)
2011-04-27 18:00:00 - 2011-04-28 03:00:00
d.
≤ 25th Percentile (n=23)
2005-09-24 14:00:00 - 2005-09-26 00:00:00
e.
PMM (n=96)
2005-09-24 14:00:00 - 2005-09-26 00:00:00
f.
≥ 75th Percentile (n=23)
2005-09-24 14:00:00 - 2005-09-26 00:00:00
g.
≤ 25th Percentile (n=234)
2011-04-04 13:00:00 - 2011-04-05 11:00:00
h.
PMM (n=1064)
2011-04-04 13:00:00 - 2011-04-05 11:00:00
i.
≥ 75th Percentile (n=252)
2011-04-04 13:00:00 - 2011-04-05 11:00:00
j.
≤ 25th Percentile (n=232)
2012-06-29 16:00:00 - 2012-06-30 06:00:00
k.
PMM (n=990)
2012-06-29 16:00:00 - 2012-06-30 06:00:00
l.
≥ 75th Percentile (n=233)
2012-06-29 16:00:00 - 2012-06-30 06:00:00
km
N
0 100 200 300 400 500
0 10 20 30 40 50 60 70 80

Figure 4. As in Figure 2, except for images affiliated with tornado reports from (a, b, c) 1800 UTC on 27 April 2011 to 0300 UTC on 28 April 2011 and (d, e, f) 1400 UTC on 24 September 2005 to 0000 UTC on 26 September 2005 and wind reports from (g, h, i) 1300 UTC on 4 April 2011 to 1100 UTC on 5 April 2011 and (j, k, l) 1600 UTC on 29 June 2012 to 0600 UTC on 30 June 2012.

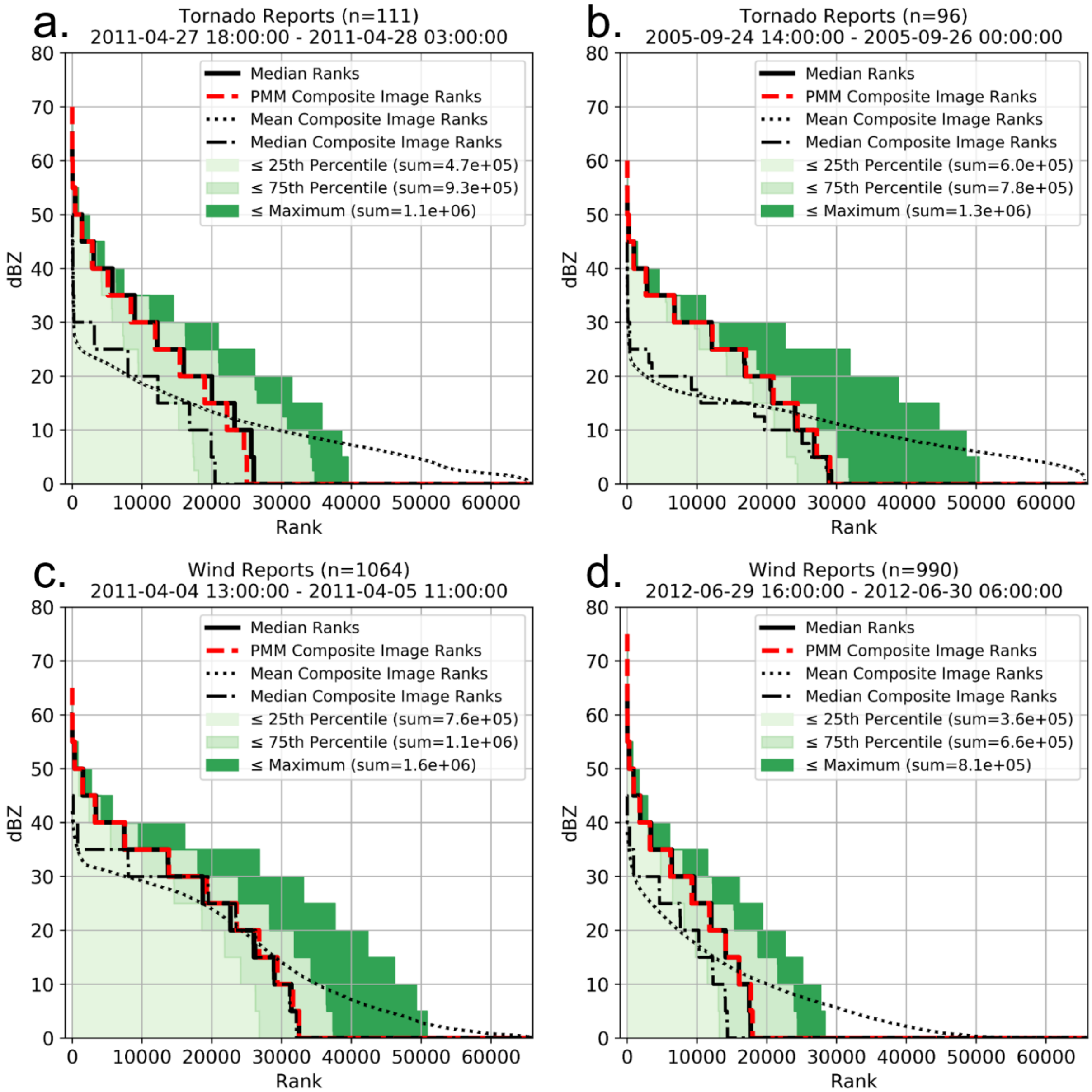

Figure 5. As in Figure 3, except for images affiliated with tornado reports from (a) 1800 UTC on 27 April 2011 to 0300 UTC on 28 April 2011 and (b) 1400 UTC on 24 September 2005 to 0000 UTC on 26 September 2005 and wind reports from (c) 1300 UTC on 4 April 2011 to 1100 UTC on 5 April 2011 and (d) 1600 UTC on 29 June 2012 to 0600 UTC on 30 June 2012.

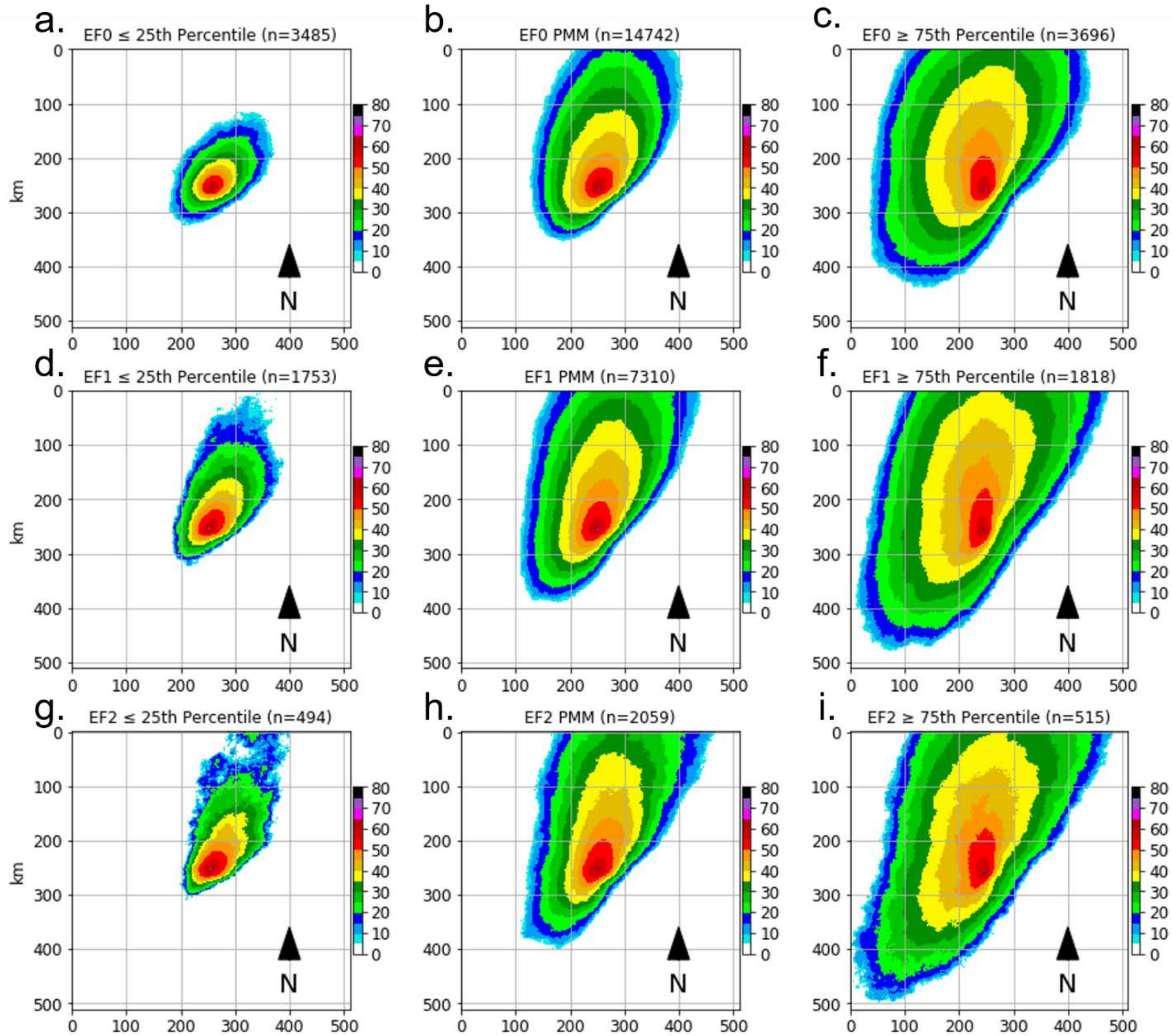

Figure 6. As in Figure 2, except for images filtered by EF-scale. Namely, only those images associated with tornadoes rated (a, b, c) EF0, (d, e, f) EF1, and (g, h, i) EF2.

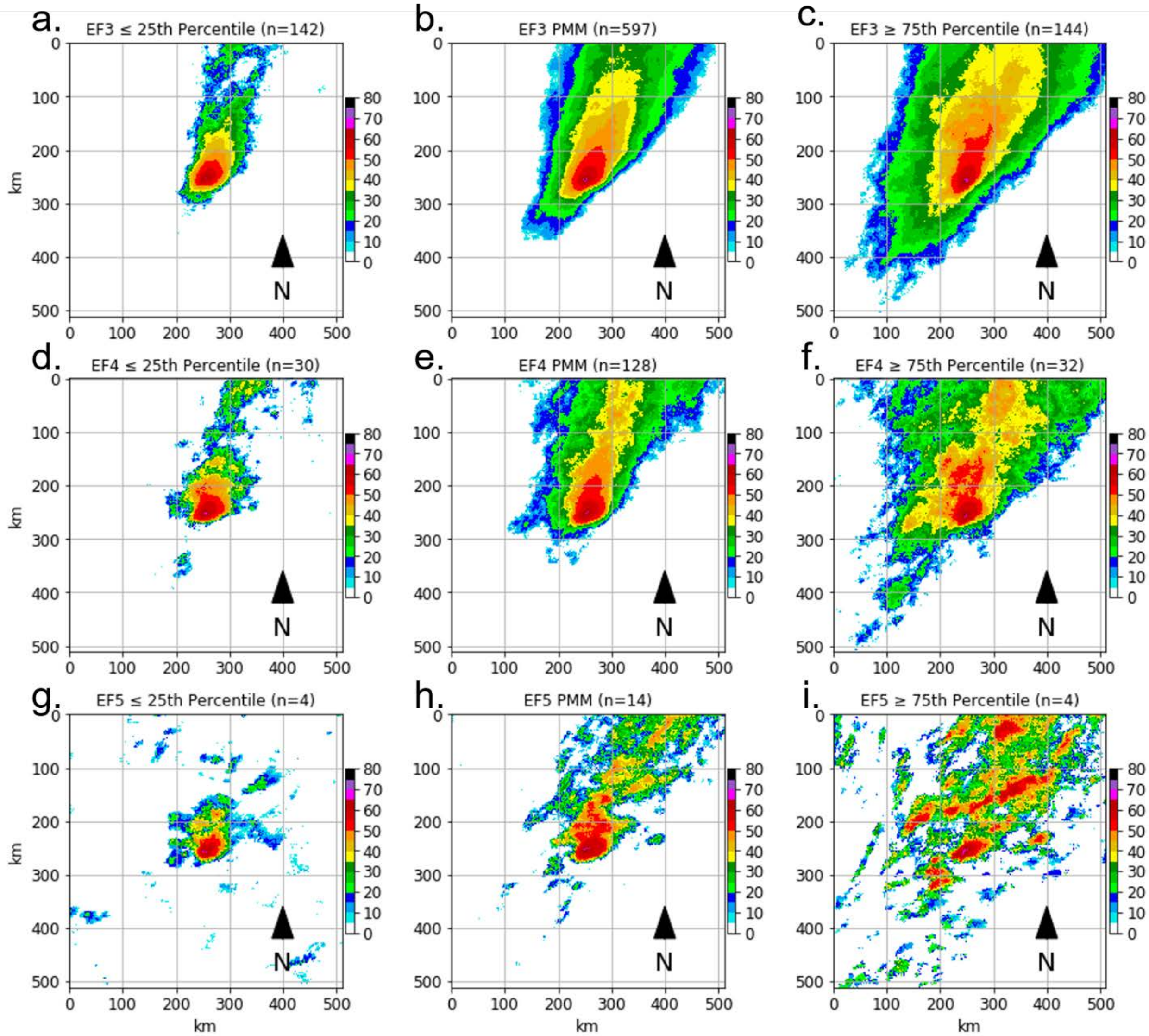

Figure 7. As in Figure 2, except for those images associated with tornadoes rated (a, b, c) EF3, (d, e, f) EF4, and (g, h, i) EF5.

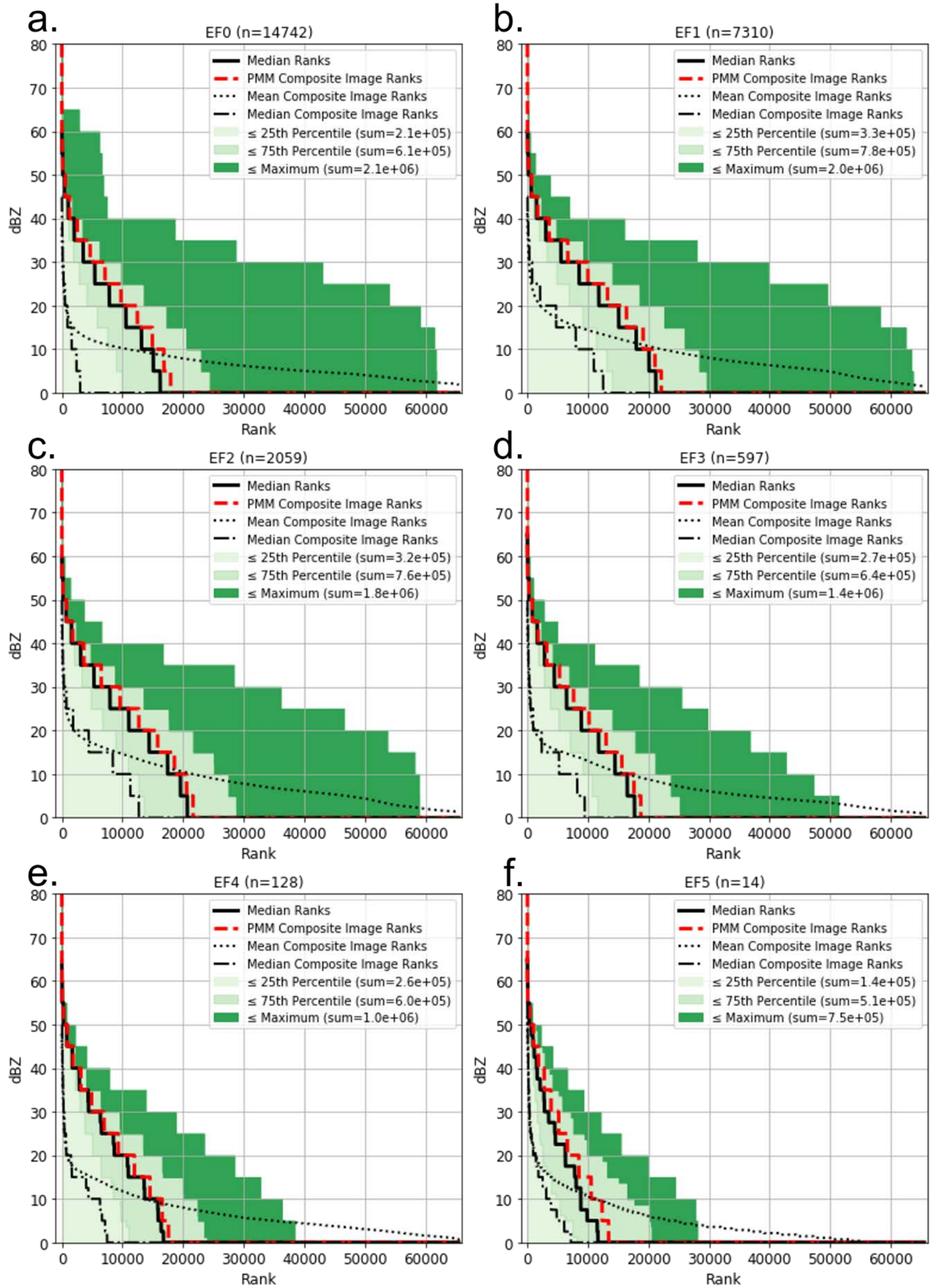

a.
EF0 (n=14742)
b.
EF1 (n=7310)
c.
EF2 (n=2059)
d.
EF3 (n=597)
e.
EF4 (n=128)
f.
EF5 (n=14)
Median Ranks
PMM Composite Image Ranks
Mean Composite Image Ranks
Median Composite Image Ranks
≤ 25th Percentile (sum=2.1e+05)
≤ 75th Percentile (sum=6.1e+05)
≤ Maximum (sum=2.1e+06)
≤ 25th Percentile (sum=3.3e+05)
≤ 75th Percentile (sum=7.8e+05)
≤ Maximum (sum=2.0e+06)
≤ 25th Percentile (sum=3.2e+05)
≤ 75th Percentile (sum=7.6e+05)
≤ Maximum (sum=1.8e+06)
≤ 25th Percentile (sum=2.7e+05)
≤ 75th Percentile (sum=6.4e+05)
≤ Maximum (sum=1.4e+06)
≤ 25th Percentile (sum=2.6e+05)
≤ 75th Percentile (sum=6.0e+05)
≤ Maximum (sum=1.0e+06)
≤ 25th Percentile (sum=1.4e+05)
≤ 75th Percentile (sum=5.1e+05)
≤ Maximum (sum=7.5e+05)
dBZ
Rank

Figure 8. As in Figure 3, except for (a) EF0, (b) EF1, (c) EF2, (d) EF3, (e) EF4, and (f) EF5 reports.

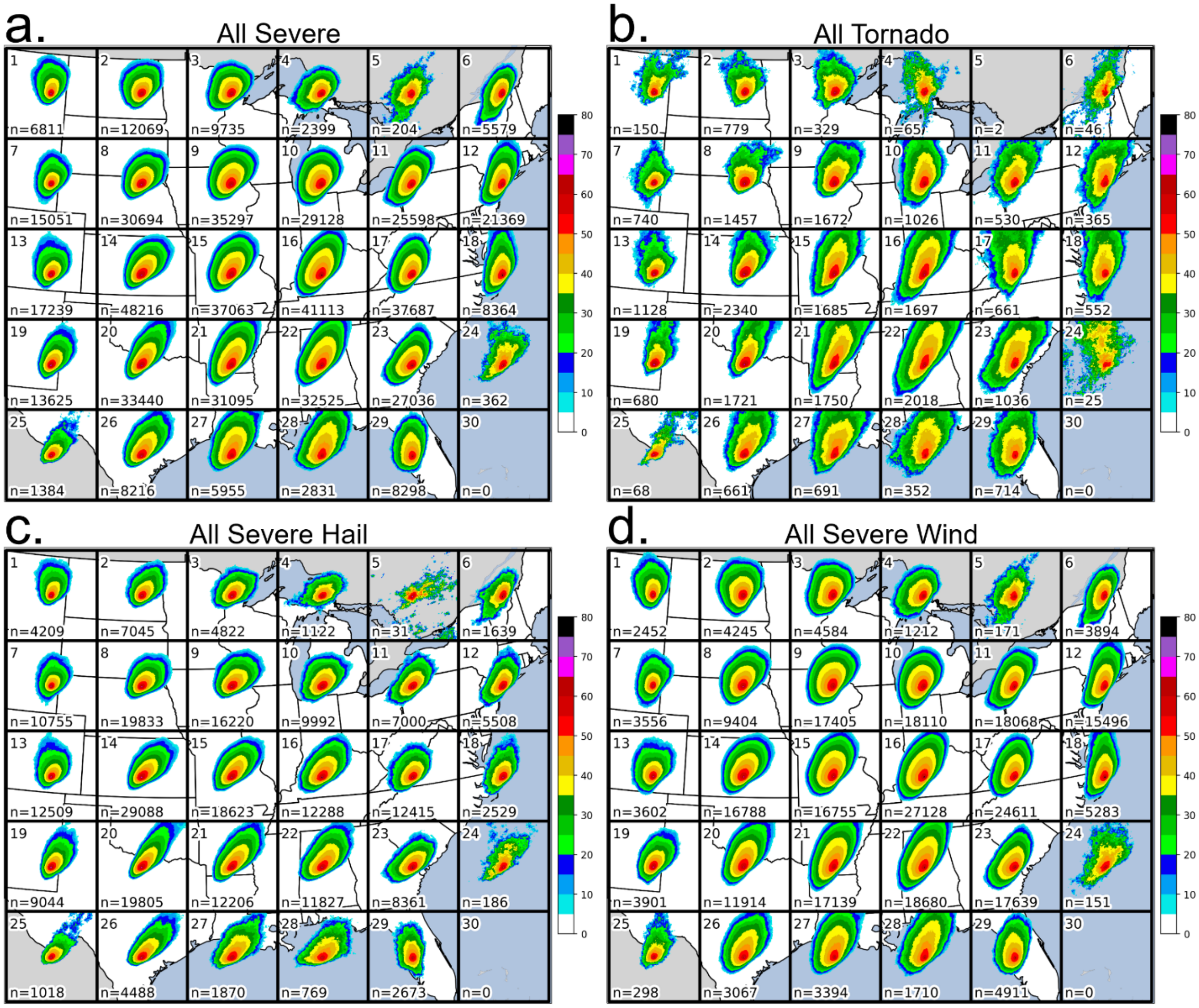

Figure 9. As in Figure 2, except for (a) all severe weather events, (b) tornado events, (c) hail events, and (d) wind events from 1996 – 2017 that are spatially filtered by grid (1-30) region. A minimum of 10 reports within a grid was necessary to plot the composites. Each box has the dimensions of 512 x 512 km.

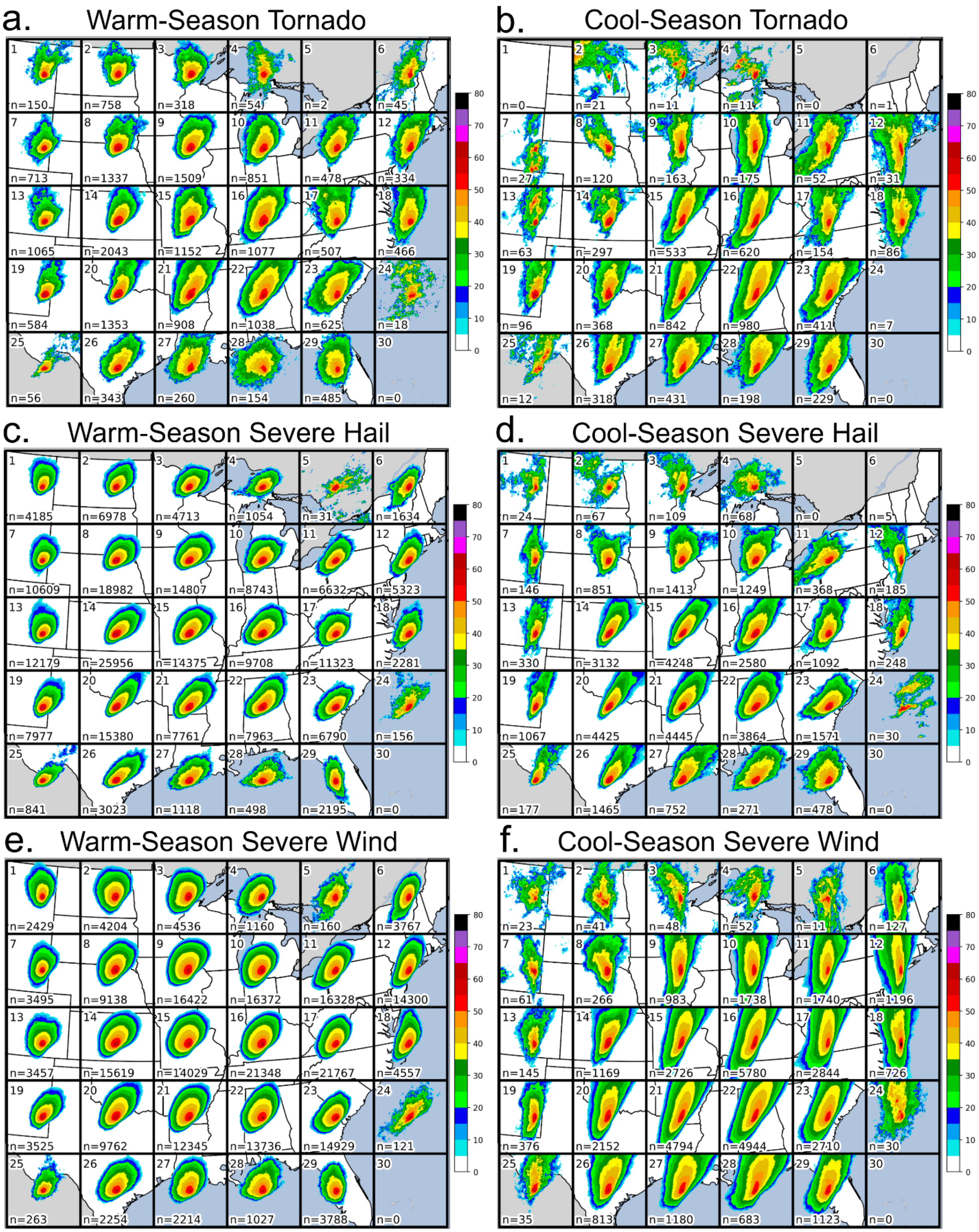
a. Warm-Season Tornado
1 n=150
2 n=758
3 n=318
4 n=54
5 n=2
6 n=45
7 n=713
8 n=1337
9 n=1509
10 n=851
11 n=478
12 n=334
13 n=1065
14 n=2043
15 n=1152
16 n=1077
17 n=507
18 n=466
19 n=584
20 n=1353
21 n=908
22 n=1038
23 n=625
24 n=18
25 n=56
26 n=343
27 n=260
28 n=154
29 n=485
30 n=0
b. Cool-Season Tornado
1 n=0
2 n=21
3 n=11
4 n=11
5 n=0
6 n=1
7 n=27
8 n=120
9 n=163
10 n=175
11 n=52
12 n=31
13 n=63
14 n=297
15 n=533
16 n=620
17 n=154
18 n=86
19 n=96
20 n=368
21 n=842
22 n=980
23 n=411
24 n=7
25 n=12
26 n=318
27 n=431
28 n=198
29 n=229
30 n=0
c. Warm-Season Severe Hail
1 n=4185
2 n=6978
3 n=4713
4 n=1054
5 n=31
6 n=1634
7 n=10609
8 n=18982
9 n=14807
10 n=8743
11 n=6632
12 n=5323
13 n=12179
14 n=25956
15 n=14375
16 n=9708
17 n=11323
18 n=2281
19 n=7977
20 n=15380
21 n=7761
22 n=7963
23 n=6790
24 n=156
25 n=841
26 n=3023
27 n=1118
28 n=498
29 n=2195
30 n=0
d. Cool-Season Severe Hail
1 n=24
2 n=67
3 n=109
4 n=68
5 n=0
6 n=5
7 n=146
8 n=851
9 n=1413
10 n=1249
11 n=368
12 n=185
13 n=330
14 n=3132
15 n=4248
16 n=2580
17 n=1092
18 n=248
19 n=1067
20 n=4425
21 n=4445
22 n=3864
23 n=1571
24 n=30
25 n=177
26 n=1465
27 n=752
28 n=271
29 n=478
30 n=0
e. Warm-Season Severe Wind
1 n=2429
2 n=4204
3 n=4536
4 n=1160
5 n=160
6 n=3767
7 n=3495
8 n=9138
9 n=16422
10 n=16372
11 n=16328
12 n=14300
13 n=3457
14 n=15619
15 n=14029
16 n=21348
17 n=21767
18 n=4557
19 n=3525
20 n=9762
21 n=12345
22 n=13736
23 n=14929
24 n=121
25 n=263
26 n=2254
27 n=2214
28 n=1027
29 n=3788
30 n=0
f. Cool-Season Severe Wind
1 n=23
2 n=41
3 n=48
4 n=52
5 n=11
6 n=127
7 n=61
8 n=266
9 n=983
10 n=1738
11 n=1740
12 n=1196
13 n=145
14 n=1169
15 n=2726
16 n=5780
17 n=2844
18 n=726
19 n=376
20 n=2152
21 n=4794
22 n=4944
23 n=2710
24 n=30
25 n=35
26 n=813
27 n=1180
28 n=683
29 n=1123
30 n=0
80
70
60
50
40
30
20
10
0

Figure 10. As in Figure 9, except for (a, c, e) warm season (April – September), and (b, d, f) cool season (October – March) for all hazard intensities.

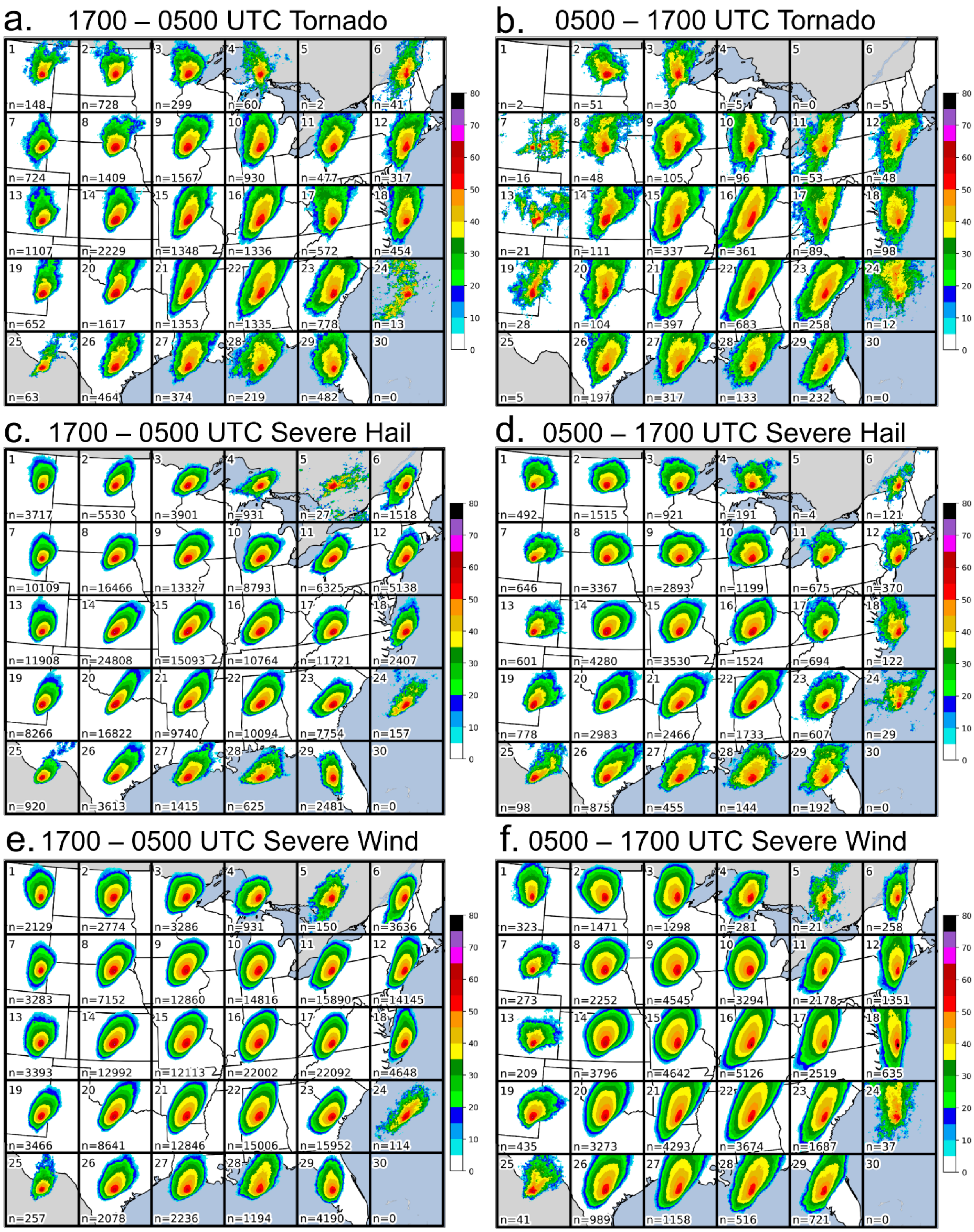
a. 1700 – 0500 UTC Tornado
b. 0500 – 1700 UTC Tornado
c. 1700 – 0500 UTC Severe Hail
d. 0500 – 1700 UTC Severe Hail
e. 1700 – 0500 UTC Severe Wind
f. 0500 – 1700 UTC Severe Wind
n=148
n=728
n=299
n=60
n=2
n=41
n=724
n=1409
n=1567
n=930
n=477
n=317
n=1107
n=2229
n=1348
n=1336
n=572
n=454
n=652
n=1617
n=1353
n=1335
n=778
n=13
n=63
n=464
n=374
n=219
n=482
n=0
n=2
n=51
n=30
n=5
n=0
n=5
n=16
n=48
n=105
n=96
n=53
n=48
n=21
n=111
n=337
n=361
n=89
n=98
n=28
n=104
n=397
n=683
n=258
n=12
n=5
n=197
n=317
n=133
n=232
n=0
n=3717
n=5530
n=3901
n=931
n=27
n=1518
n=10109
n=16466
n=13327
n=8793
n=6325
n=5138
n=11908
n=24808
n=15093
n=10764
n=11721
n=2407
n=8266
n=16822
n=9740
n=10094
n=7754
n=157
n=920
n=3613
n=1415
n=625
n=2481
n=0
n=492
n=1515
n=921
n=191
n=4
n=121
n=646
n=3367
n=2893
n=1199
n=675
n=370
n=601
n=4280
n=3530
n=1524
n=694
n=122
n=778
n=2983
n=2466
n=1733
n=607
n=29
n=98
n=875
n=455
n=144
n=192
n=0
n=2129
n=2774
n=3286
n=931
n=150
n=3636
n=3283
n=7152
n=12860
n=14816
n=15890
n=14145
n=3393
n=12992
n=12113
n=22002
n=22092
n=4648
n=3466
n=8641
n=12846
n=15006
n=15952
n=114
n=257
n=2078
n=2236
n=1194
n=4190
n=0
n=323
n=1471
n=1298
n=281
n=21
n=258
n=273
n=2252
n=4545
n=3294
n=2178
n=1351
n=209
n=3796
n=4642
n=5126
n=2519
n=635
n=435
n=3273
n=4293
n=3674
n=1687
n=37
n=41
n=989
n=1158
n=516
n=721
n=0
80
70
60
50
40
30
20
10
0

Figure 11. As in Figure 9, except for (a, c, e) “afternoon and early evening” (1700 - 0500 UTC), and (b, d, f) “night and morning” (0500 – 1700 UTC). For each period, the ending time is not included in that subset.

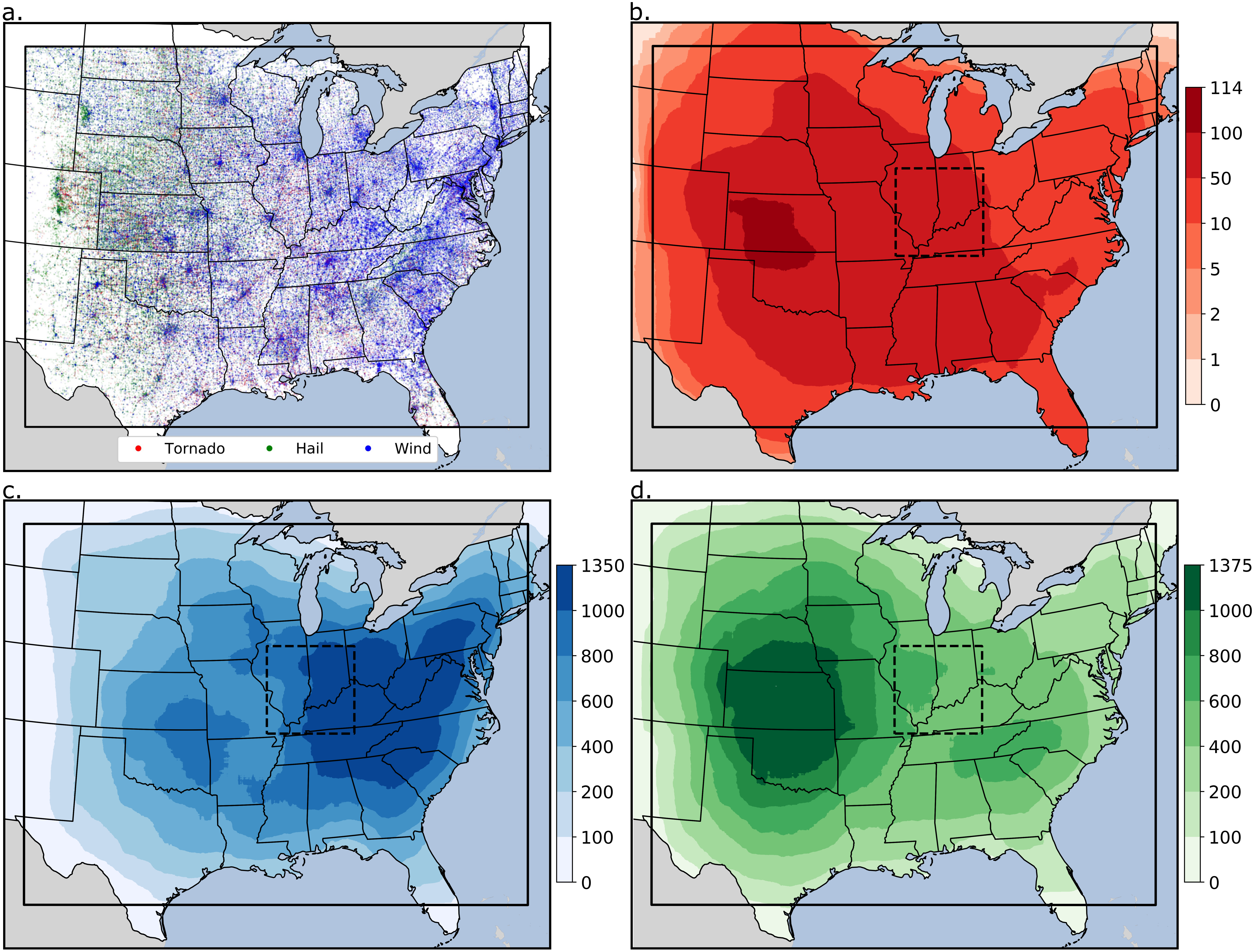

a.
Tornado
Hail
Wind
b.
114
100
50
10
5
2
1
0
c.
1350
1000
800
600
400
200
100
0
d.
1375
1000
800
600
400
200
100
0

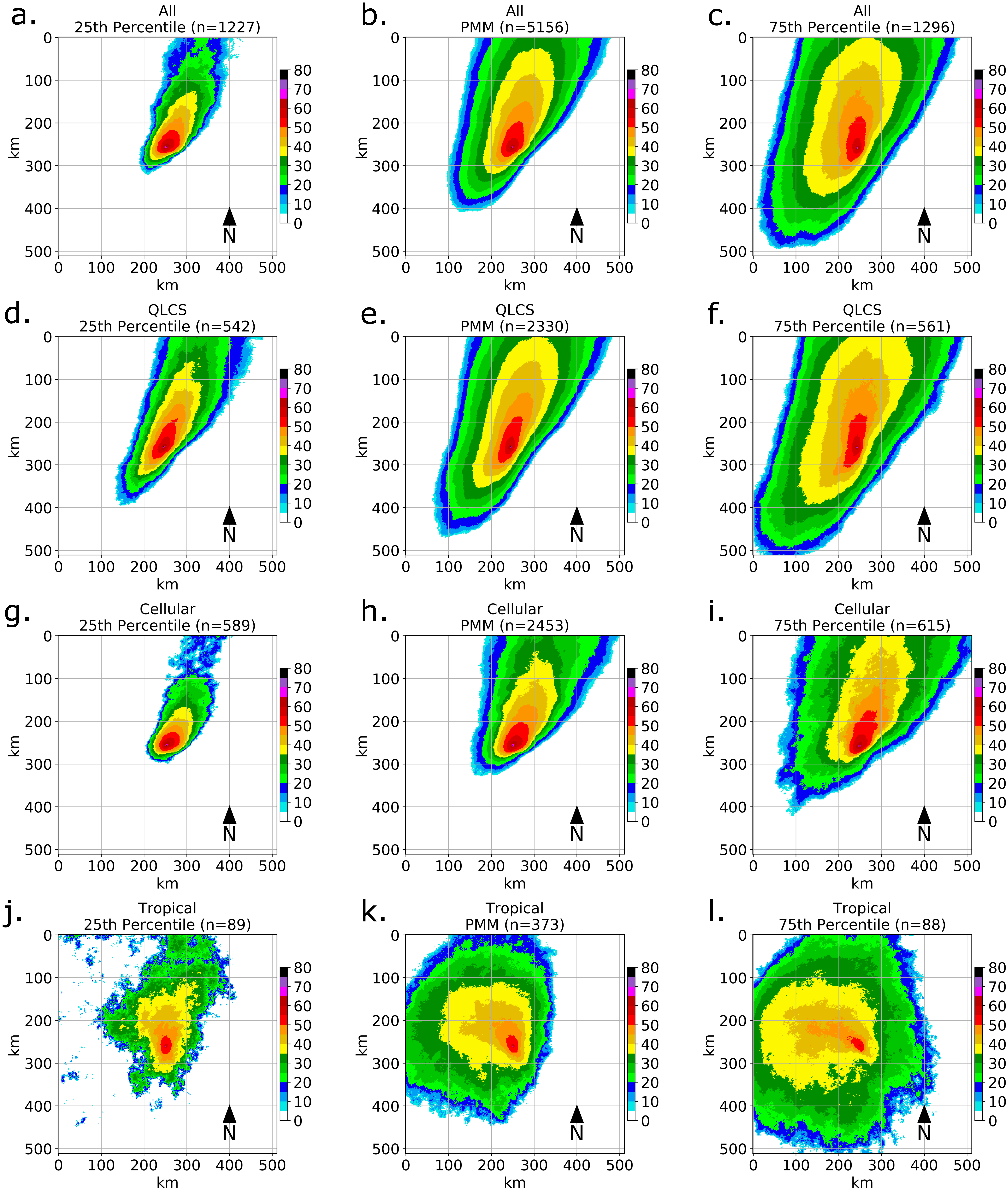
a.
All
25th Percentile (n=1227)
b.
All
PMM (n=5156)
c.
All
75th Percentile (n=1296)
d.
QLCS
25th Percentile (n=542)
e.
QLCS
PMM (n=2330)
f.
QLCS
75th Percentile (n=561)
g.
Cellular
25th Percentile (n=589)
h.
Cellular
PMM (n=2453)
i.
Cellular
75th Percentile (n=615)
j.
Tropical
25th Percentile (n=89)
k.
Tropical
PMM (n=373)
l.
Tropical
75th Percentile (n=88)
km
N

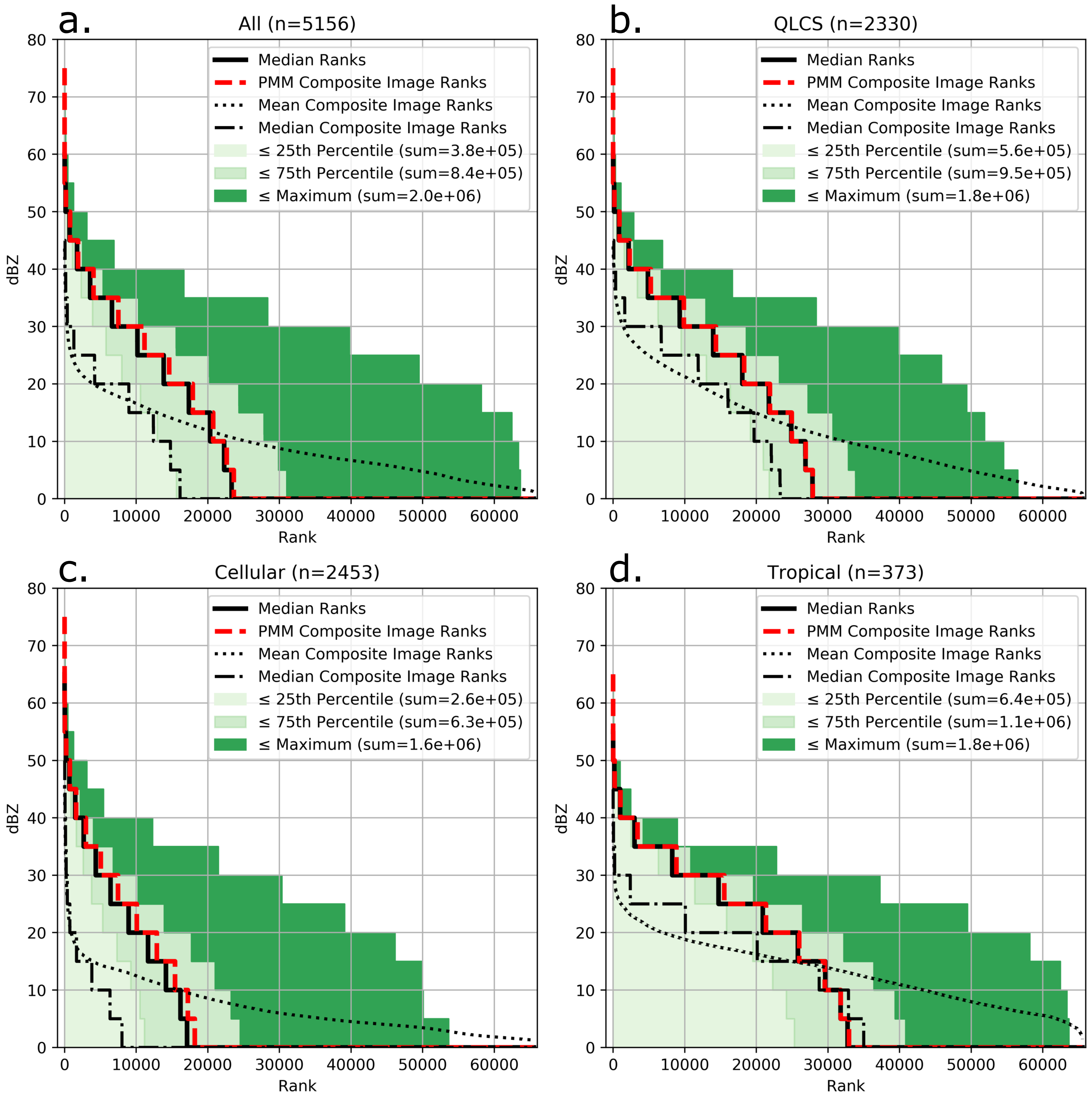

a.
All (n=5156)
b.
QLCS (n=2330)
c.
Cellular (n=2453)
d.
Tropical (n=373)
Median Ranks
PMM Composite Image Ranks
Mean Composite Image Ranks
Median Composite Image Ranks
≤ 25th Percentile (sum=3.8e+05)
≤ 75th Percentile (sum=8.4e+05)
≤ Maximum (sum=2.0e+06)
≤ 25th Percentile (sum=5.6e+05)
≤ 75th Percentile (sum=9.5e+05)
≤ Maximum (sum=1.8e+06)
≤ 25th Percentile (sum=2.6e+05)
≤ 75th Percentile (sum=6.3e+05)
≤ Maximum (sum=1.6e+06)
≤ 25th Percentile (sum=6.4e+05)
≤ 75th Percentile (sum=1.1e+06)
≤ Maximum (sum=1.8e+06)
dBZ
Rank

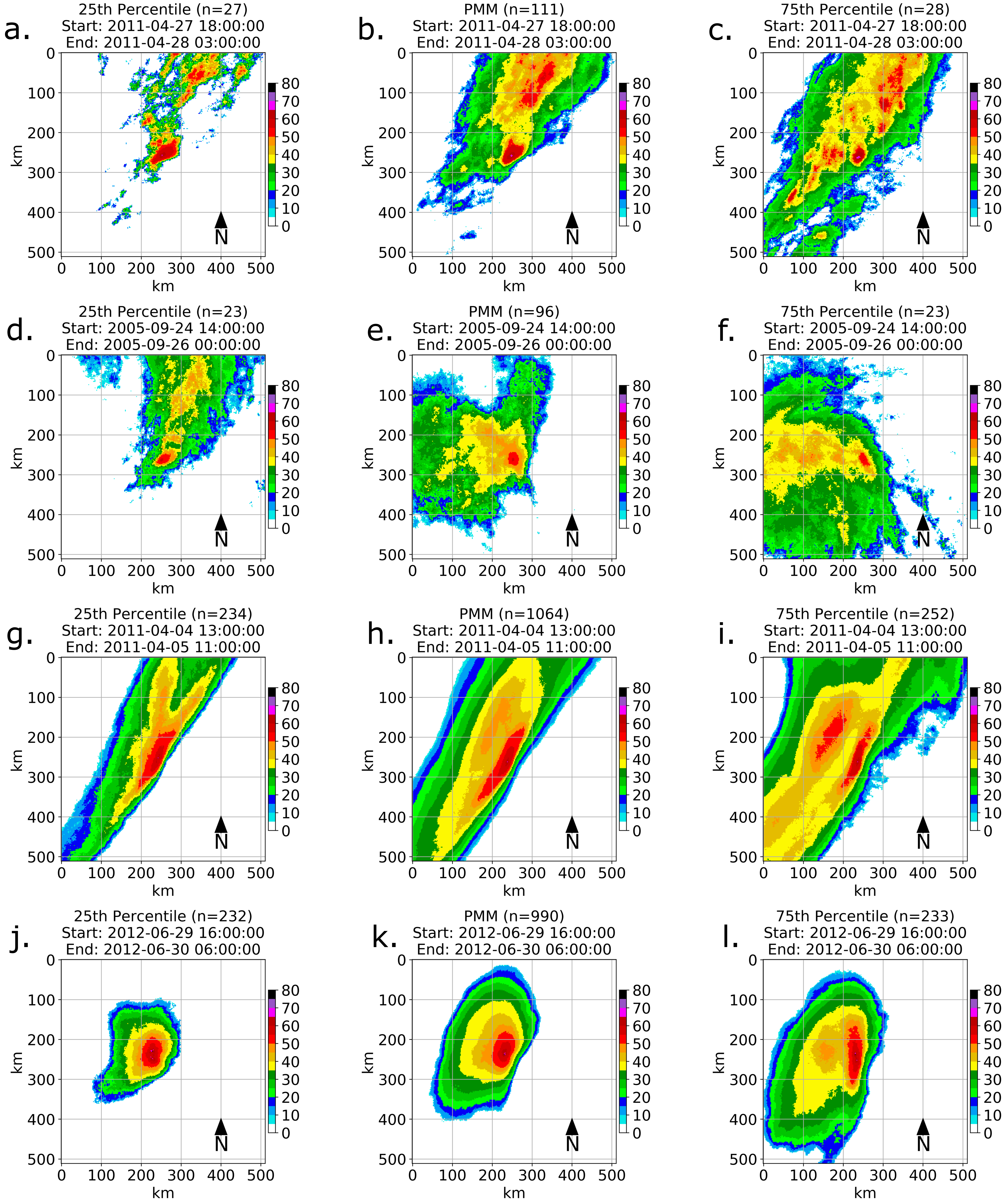
a.
25th Percentile (n=27)
Start: 2011-04-27 18:00:00
End: 2011-04-28 03:00:00
b.
PMM (n=111)
Start: 2011-04-27 18:00:00
End: 2011-04-28 03:00:00
c.
75th Percentile (n=28)
Start: 2011-04-27 18:00:00
End: 2011-04-28 03:00:00
d.
25th Percentile (n=23)
Start: 2005-09-24 14:00:00
End: 2005-09-26 00:00:00
e.
PMM (n=96)
Start: 2005-09-24 14:00:00
End: 2005-09-26 00:00:00
f.
75th Percentile (n=23)
Start: 2005-09-24 14:00:00
End: 2005-09-26 00:00:00
g.
25th Percentile (n=234)
Start: 2011-04-04 13:00:00
End: 2011-04-05 11:00:00
h.
PMM (n=1064)
Start: 2011-04-04 13:00:00
End: 2011-04-05 11:00:00
i.
75th Percentile (n=252)
Start: 2011-04-04 13:00:00
End: 2011-04-05 11:00:00
j.
25th Percentile (n=232)
Start: 2012-06-29 16:00:00
End: 2012-06-30 06:00:00
k.
PMM (n=990)
Start: 2012-06-29 16:00:00
End: 2012-06-30 06:00:00
l.
75th Percentile (n=233)
Start: 2012-06-29 16:00:00
End: 2012-06-30 06:00:00
km
0 100 200 300 400 500
N
0 10 20 30 40 50 60 70 80

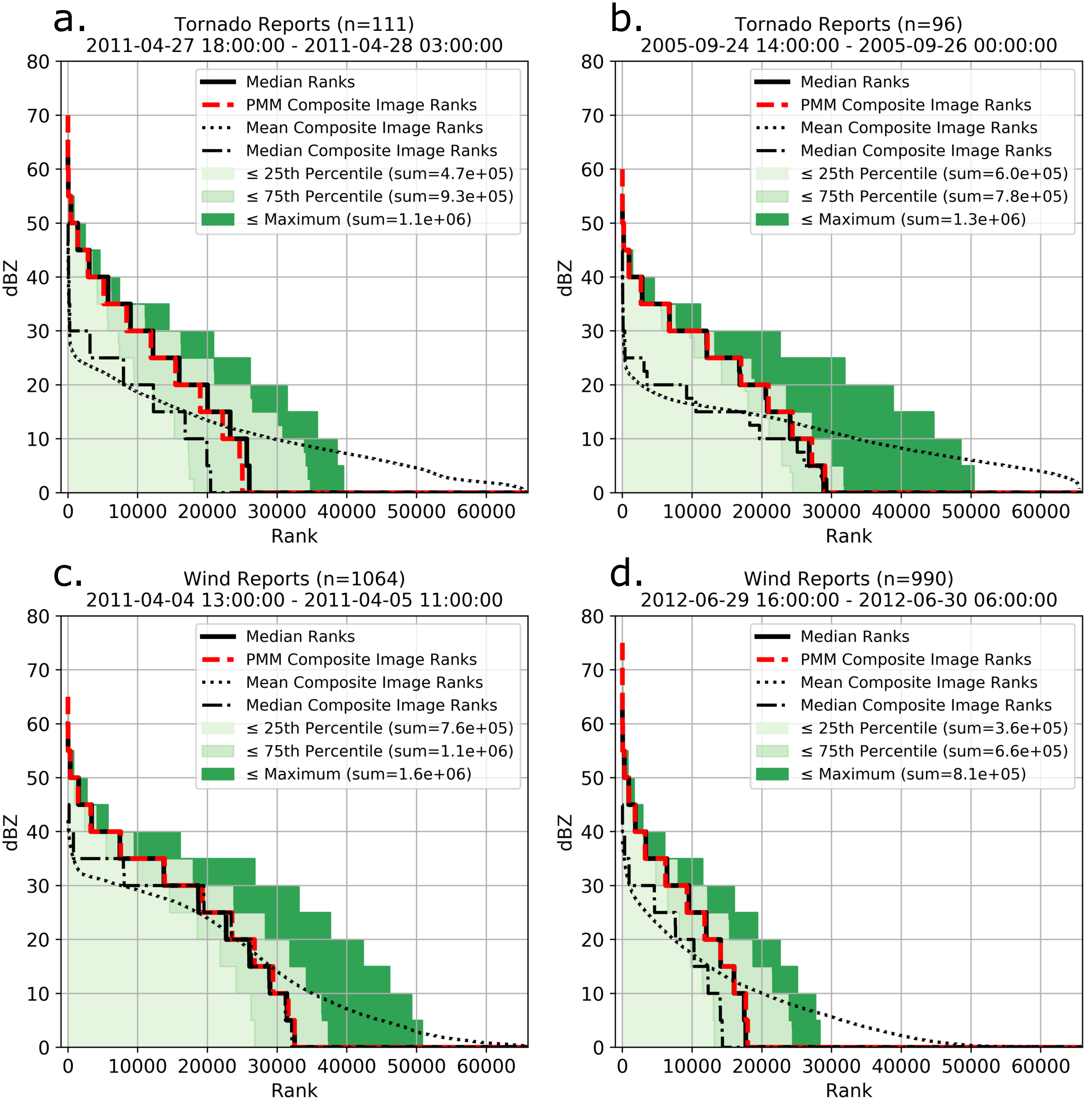
a.
Tornado Reports (n=111)
2011-04-27 18:00:00 - 2011-04-28 03:00:00
b.
Tornado Reports (n=96)
2005-09-24 14:00:00 - 2005-09-26 00:00:00
c.
Wind Reports (n=1064)
2011-04-04 13:00:00 - 2011-04-05 11:00:00
d.
Wind Reports (n=990)
2012-06-29 16:00:00 - 2012-06-30 06:00:00
Median Ranks
PMM Composite Image Ranks
Mean Composite Image Ranks
Median Composite Image Ranks
≤ 25th Percentile (sum=4.7e+05)
≤ 75th Percentile (sum=9.3e+05)
≤ Maximum (sum=1.1e+06)
≤ 25th Percentile (sum=6.0e+05)
≤ 75th Percentile (sum=7.8e+05)
≤ Maximum (sum=1.3e+06)
≤ 25th Percentile (sum=7.6e+05)
≤ 75th Percentile (sum=1.1e+06)
≤ Maximum (sum=1.6e+06)
≤ 25th Percentile (sum=3.6e+05)
≤ 75th Percentile (sum=6.6e+05)
≤ Maximum (sum=8.1e+05)
dBZ
Rank

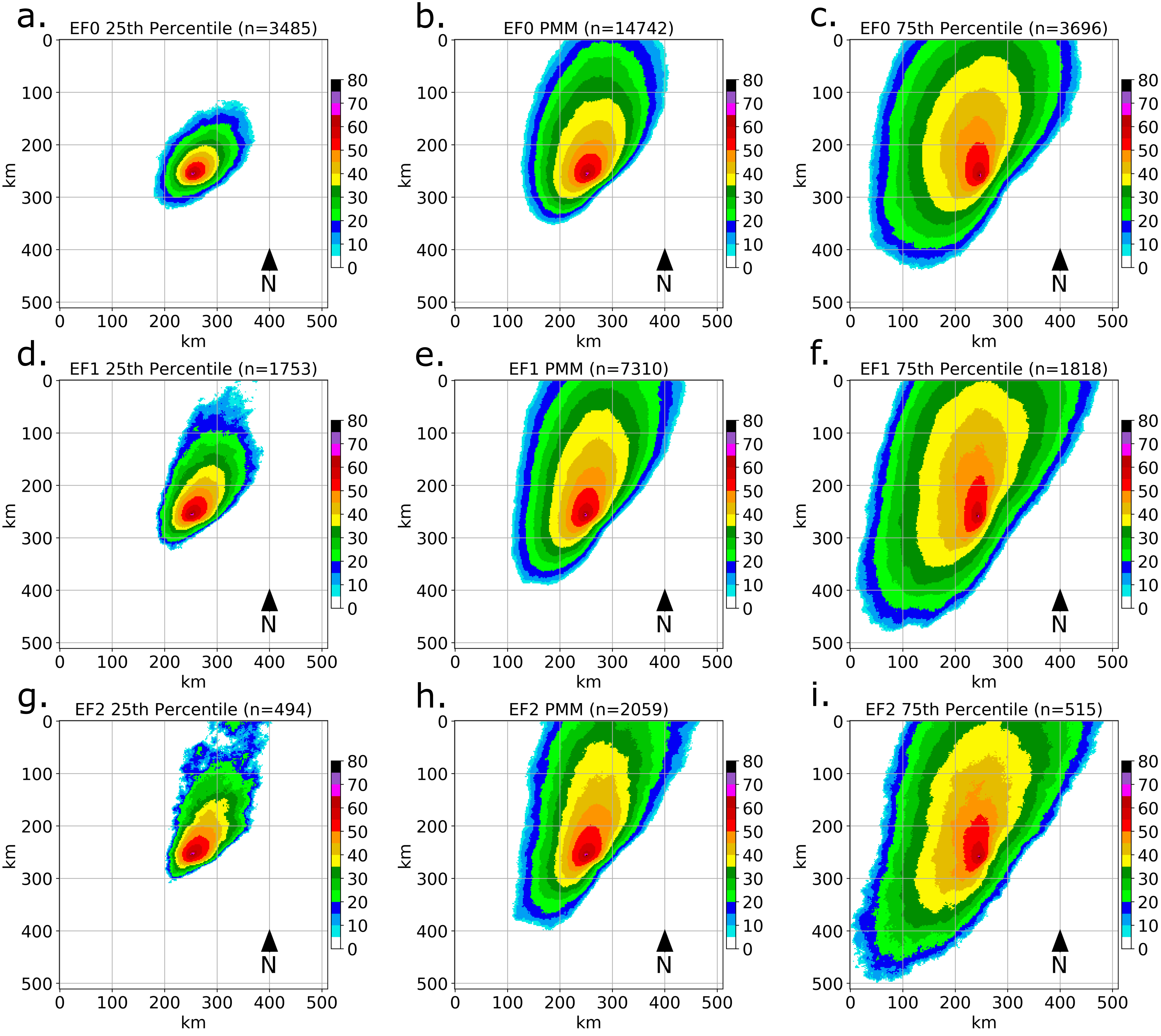
a.
EF0 25th Percentile (n=3485)
b.
EF0 PMM (n=14742)
c.
EF0 75th Percentile (n=3696)
d.
EF1 25th Percentile (n=1753)
e.
EF1 PMM (n=7310)
f.
EF1 75th Percentile (n=1818)
g.
EF2 25th Percentile (n=494)
h.
EF2 PMM (n=2059)
i.
EF2 75th Percentile (n=515)
km
km
N
0
100
200
300
400
500
0
10
20
30
40
50
60
70
80

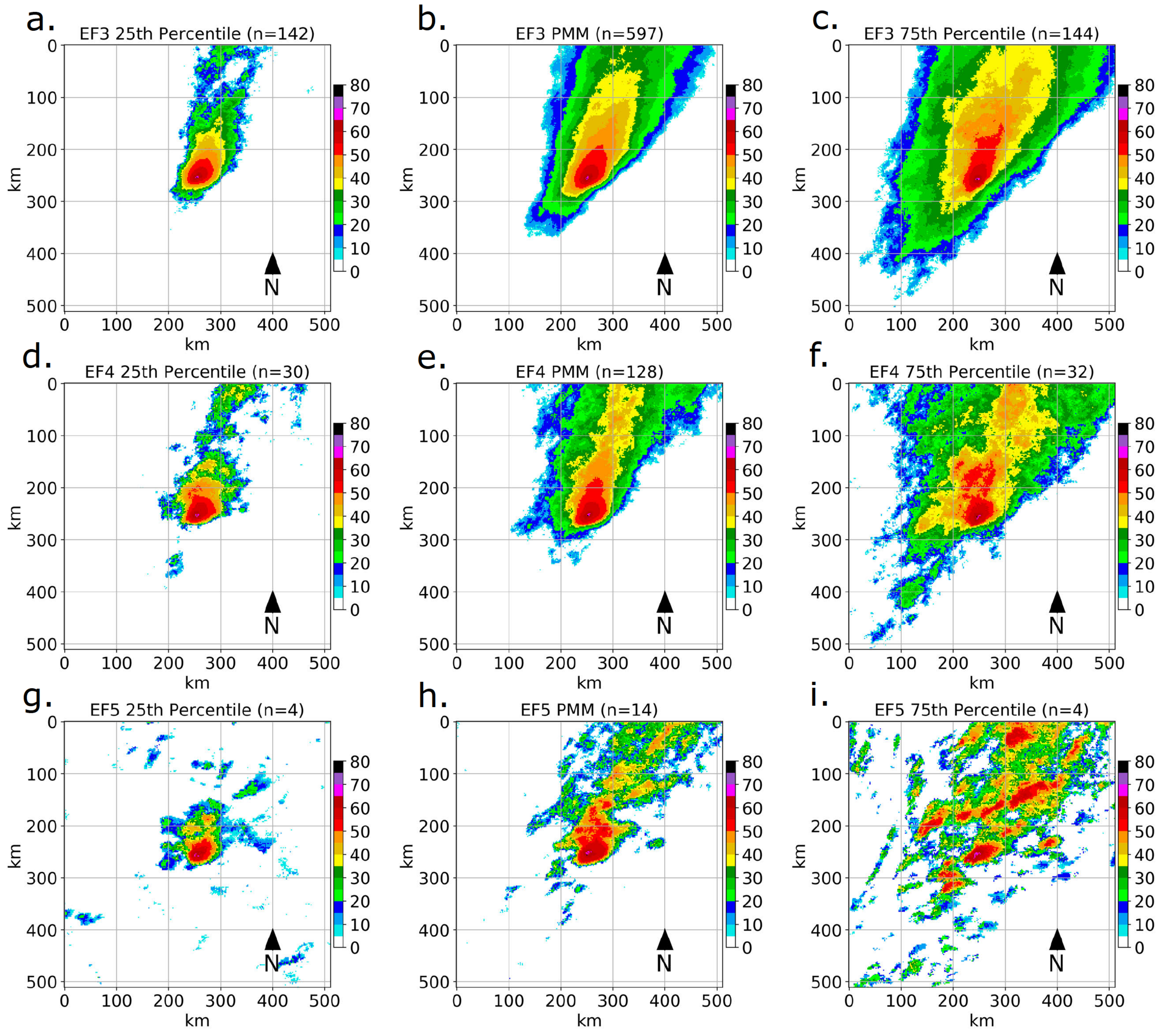
a.
EF3 25th Percentile (n=142)
b.
EF3 PMM (n=597)
c.
EF3 75th Percentile (n=144)
d.
EF4 25th Percentile (n=30)
e.
EF4 PMM (n=128)
f.
EF4 75th Percentile (n=32)
g.
EF5 25th Percentile (n=4)
h.
EF5 PMM (n=14)
i.
EF5 75th Percentile (n=4)
km
N
0
100
200
300
400
500
10
20
30
40
50
60
70
80

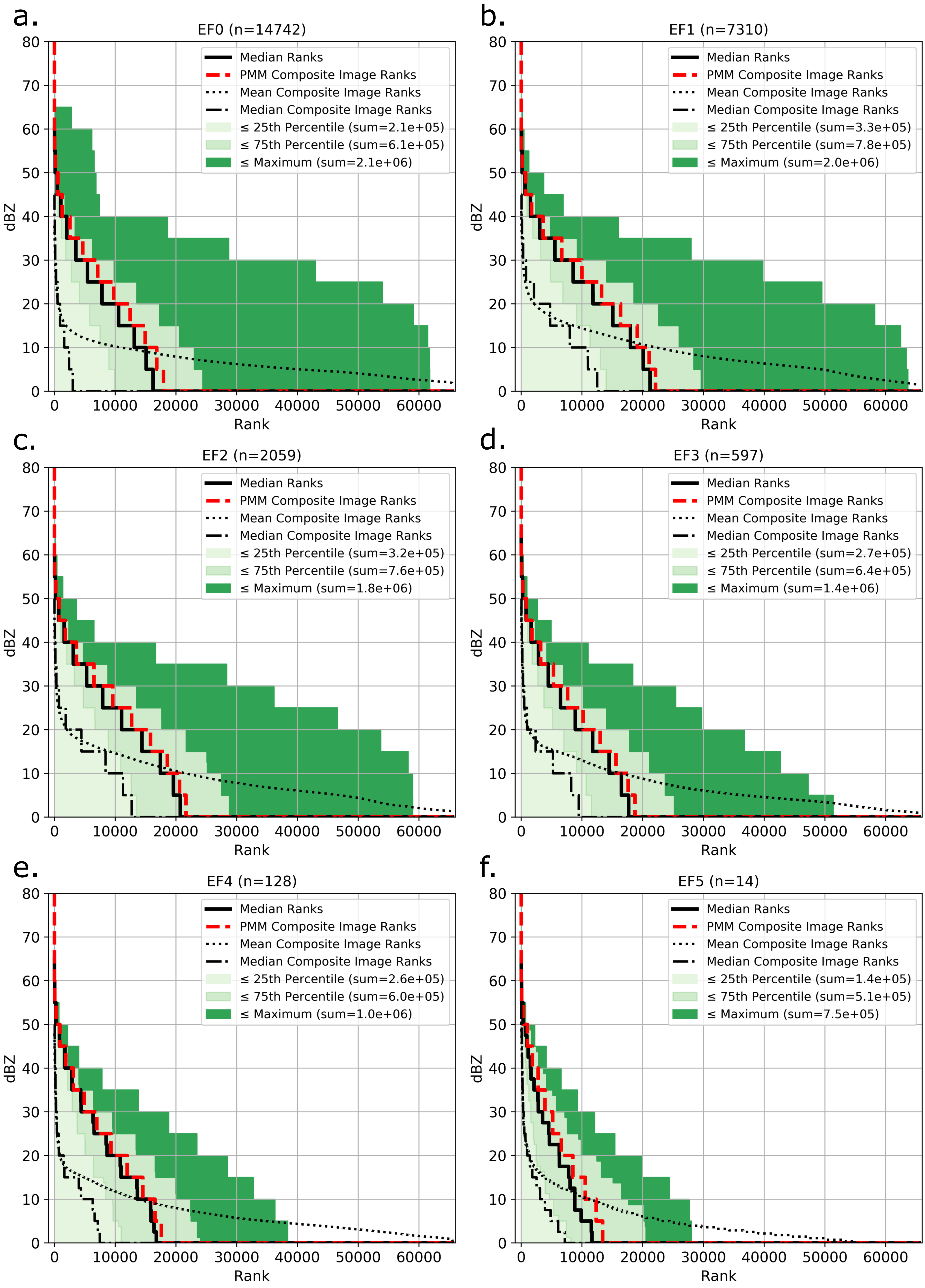
a.
EF0 (n=14742)
b.
EF1 (n=7310)
c.
EF2 (n=2059)
d.
EF3 (n=597)
e.
EF4 (n=128)
f.
EF5 (n=14)
Median Ranks
PMM Composite Image Ranks
Mean Composite Image Ranks
Median Composite Image Ranks
≤ 25th Percentile (sum=2.1e+05)
≤ 75th Percentile (sum=6.1e+05)
≤ Maximum (sum=2.1e+06)
≤ 25th Percentile (sum=3.3e+05)
≤ 75th Percentile (sum=7.8e+05)
≤ Maximum (sum=2.0e+06)
≤ 25th Percentile (sum=3.2e+05)
≤ 75th Percentile (sum=7.6e+05)
≤ Maximum (sum=1.8e+06)
≤ 25th Percentile (sum=2.7e+05)
≤ 75th Percentile (sum=6.4e+05)
≤ Maximum (sum=1.4e+06)
≤ 25th Percentile (sum=2.6e+05)
≤ 75th Percentile (sum=6.0e+05)
≤ Maximum (sum=1.0e+06)
≤ 25th Percentile (sum=1.4e+05)
≤ 75th Percentile (sum=5.1e+05)
≤ Maximum (sum=7.5e+05)
dBZ
Rank

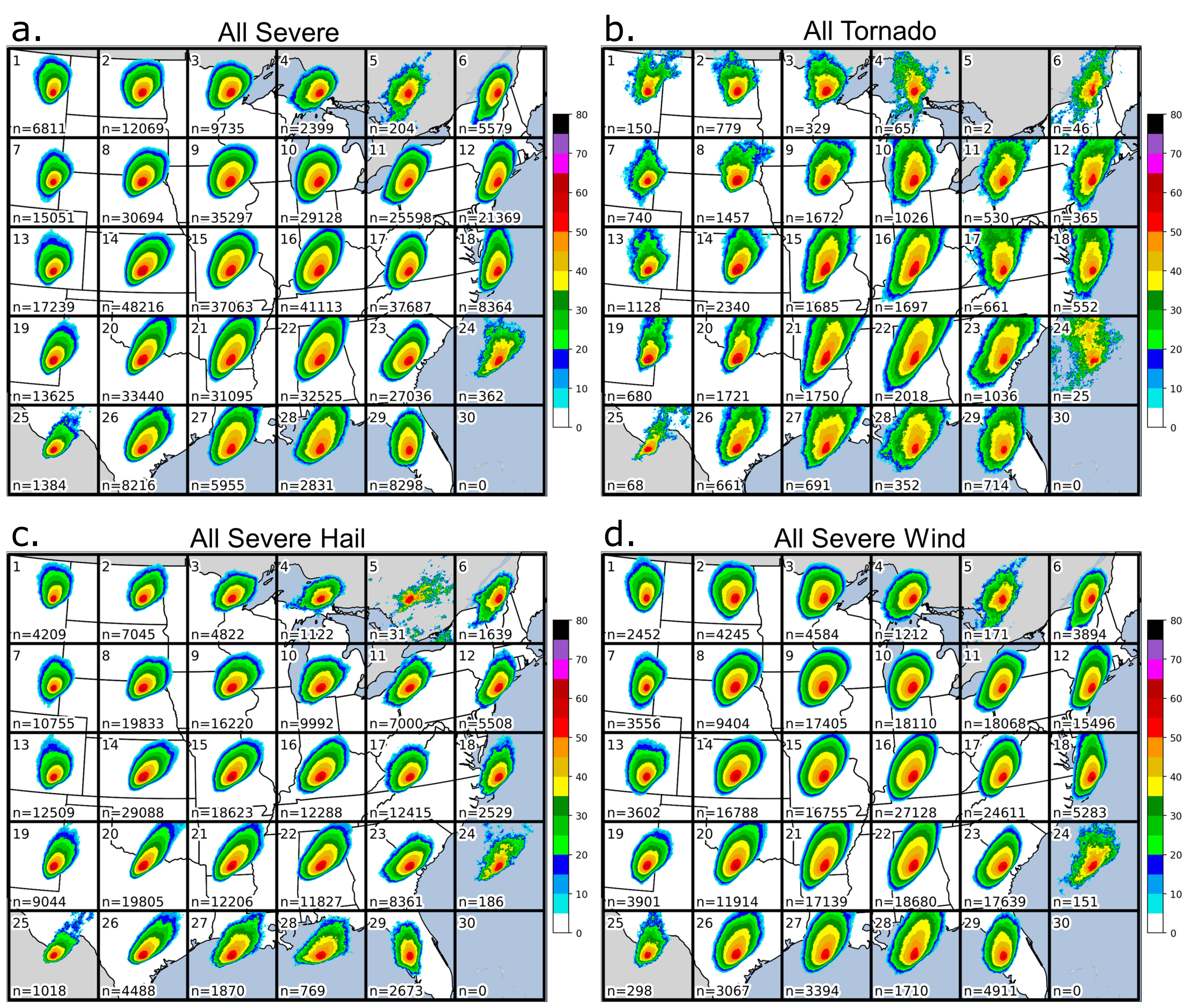
a.
All Severe
1 n=6811
2 n=12069
3 n=9735
4 n=2399
5 n=204
6 n=5579
7 n=15051
8 n=30694
9 n=35297
10 n=29128
11 n=25598
12 n=21369
13 n=17239
14 n=48216
15 n=37063
16 n=41113
17 n=37687
18 n=8364
19 n=13625
20 n=33440
21 n=31095
22 n=32525
23 n=27036
24 n=362
25 n=1384
26 n=8216
27 n=5955
28 n=2831
29 n=8298
30 n=0
80 70 60 50 40 30 20 10 0
b.
All Tornado
1 n=150
2 n=779
3 n=329
4 n=65
5 n=2
6 n=46
7 n=740
8 n=1457
9 n=1672
10 n=1026
11 n=530
12 n=365
13 n=1128
14 n=2340
15 n=1685
16 n=1697
17 n=661
18 n=552
19 n=680
20 n=1721
21 n=1750
22 n=2018
23 n=1036
24 n=25
25 n=68
26 n=661
27 n=691
28 n=352
29 n=714
30 n=0
80 70 60 50 40 30 20 10 0
c.
All Severe Hail
1 n=4209
2 n=7045
3 n=4822
4 n=1122
5 n=31
6 n=1639
7 n=10755
8 n=19833
9 n=16220
10 n=9992
11 n=7000
12 n=5508
13 n=12509
14 n=29088
15 n=18623
16 n=12288
17 n=12415
18 n=2529
19 n=9044
20 n=19805
21 n=12206
22 n=11827
23 n=8361
24 n=186
25 n=1018
26 n=4488
27 n=1870
28 n=769
29 n=2673
30 n=0
80 70 60 50 40 30 20 10 0
d.
All Severe Wind
1 n=2452
2 n=4245
3 n=4584
4 n=1212
5 n=171
6 n=3894
7 n=3556
8 n=9404
9 n=17405
10 n=18110
11 n=18068
12 n=15496
13 n=3602
14 n=16788
15 n=16755
16 n=27128
17 n=24611
18 n=5283
19 n=3901
20 n=11914
21 n=17139
22 n=18680
23 n=17639
24 n=151
25 n=298
26 n=3067
27 n=3394
28 n=1710
29 n=4911
30 n=0
80 70 60 50 40 30 20 10 0

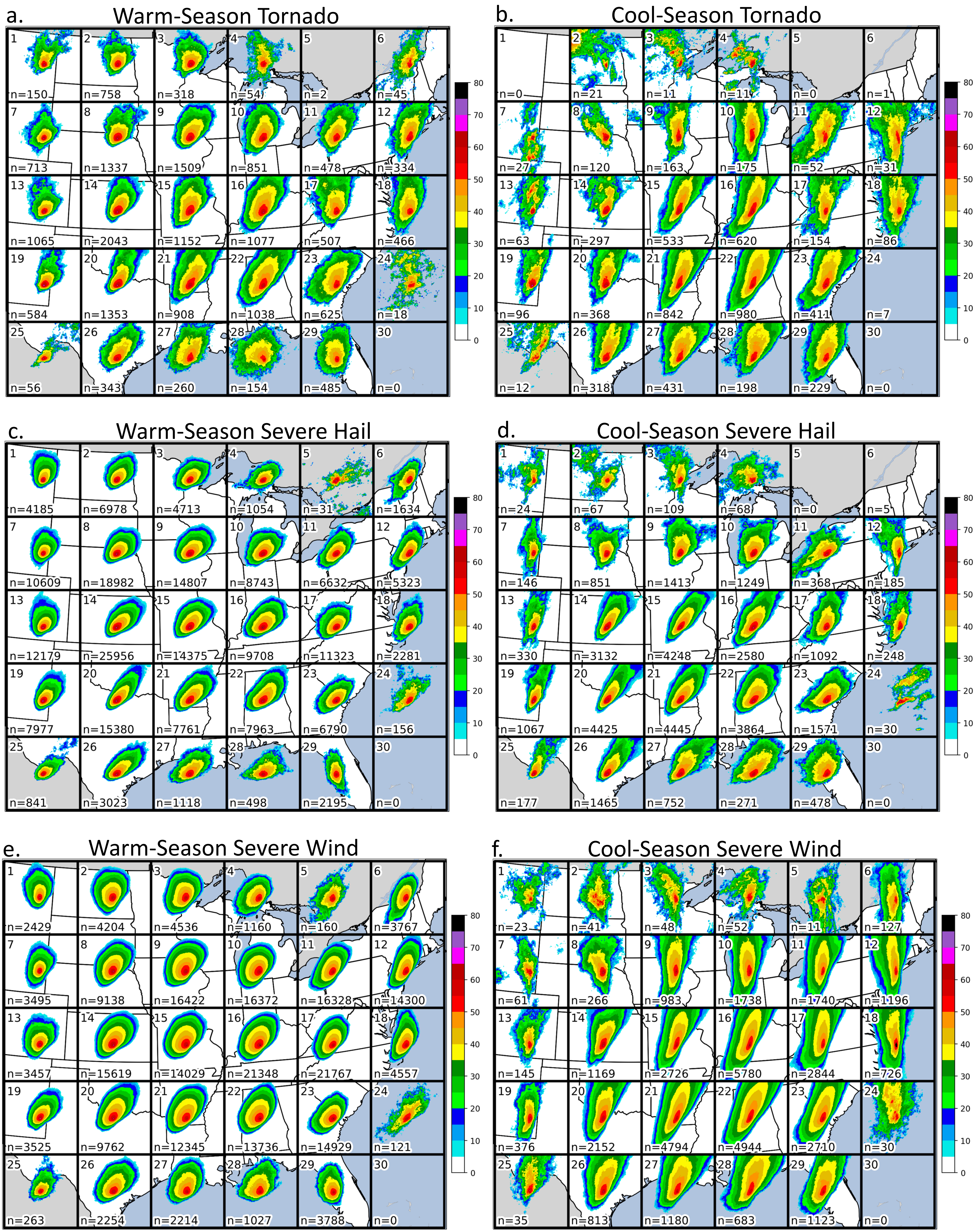
a. Warm-Season Tornado
1 n=150 2 n=758 3 n=318 4 n=54 5 n=2 6 n=45
7 n=713 8 n=1337 9 n=1509 10 n=851 11 n=478 12 n=334
13 n=1065 14 n=2043 15 n=1152 16 n=1077 17 n=507 18 n=466
19 n=584 20 n=1353 21 n=908 22 n=1038 23 n=625 24 n=18
25 n=56 26 n=343 27 n=260 28 n=154 29 n=485 30 n=0
b. Cool-Season Tornado
1 n=0 2 n=21 3 n=11 4 n=11 5 n=0 6 n=1
7 n=27 8 n=120 9 n=163 10 n=175 11 n=52 12 n=31
13 n=63 14 n=297 15 n=533 16 n=620 17 n=154 18 n=86
19 n=96 20 n=368 21 n=842 22 n=980 23 n=411 24 n=7
25 n=12 26 n=318 27 n=431 28 n=198 29 n=229 30 n=0
c. Warm-Season Severe Hail
1 n=4185 2 n=6978 3 n=4713 4 n=1054 5 n=31 6 n=1634
7 n=10609 8 n=18982 9 n=14807 10 n=8743 11 n=6632 12 n=5323
13 n=12179 14 n=25956 15 n=14375 16 n=9708 17 n=11323 18 n=2281
19 n=7977 20 n=15380 21 n=7761 22 n=7963 23 n=6790 24 n=156
25 n=841 26 n=3023 27 n=1118 28 n=498 29 n=2195 30 n=0
d. Cool-Season Severe Hail
1 n=24 2 n=67 3 n=109 4 n=68 5 n=0 6 n=5
7 n=146 8 n=851 9 n=1413 10 n=1249 11 n=368 12 n=185
13 n=330 14 n=3132 15 n=4248 16 n=2580 17 n=1092 18 n=248
19 n=1067 20 n=4425 21 n=4445 22 n=3864 23 n=1571 24 n=30
25 n=177 26 n=1465 27 n=752 28 n=271 29 n=478 30 n=0
e. Warm-Season Severe Wind
1 n=2429 2 n=4204 3 n=4536 4 n=1160 5 n=160 6 n=3767
7 n=3495 8 n=9138 9 n=16422 10 n=16372 11 n=16328 12 n=14300
13 n=3457 14 n=15619 15 n=14029 16 n=21348 17 n=21767 18 n=4557
19 n=3525 20 n=9762 21 n=12345 22 n=13736 23 n=14929 24 n=121
25 n=263 26 n=2254 27 n=2214 28 n=1027 29 n=3788 30 n=0
f. Cool-Season Severe Wind
1 n=23 2 n=41 3 n=48 4 n=52 5 n=11 6 n=127
7 n=61 8 n=266 9 n=983 10 n=1738 11 n=1740 12 n=1196
13 n=145 14 n=1169 15 n=2726 16 n=5780 17 n=2844 18 n=726
19 n=376 20 n=2152 21 n=4794 22 n=4944 23 n=2710 24 n=30
25 n=35 26 n=813 27 n=1180 28 n=683 29 n=1123 30 n=0
0 10 20 30 40 50 60 70 80

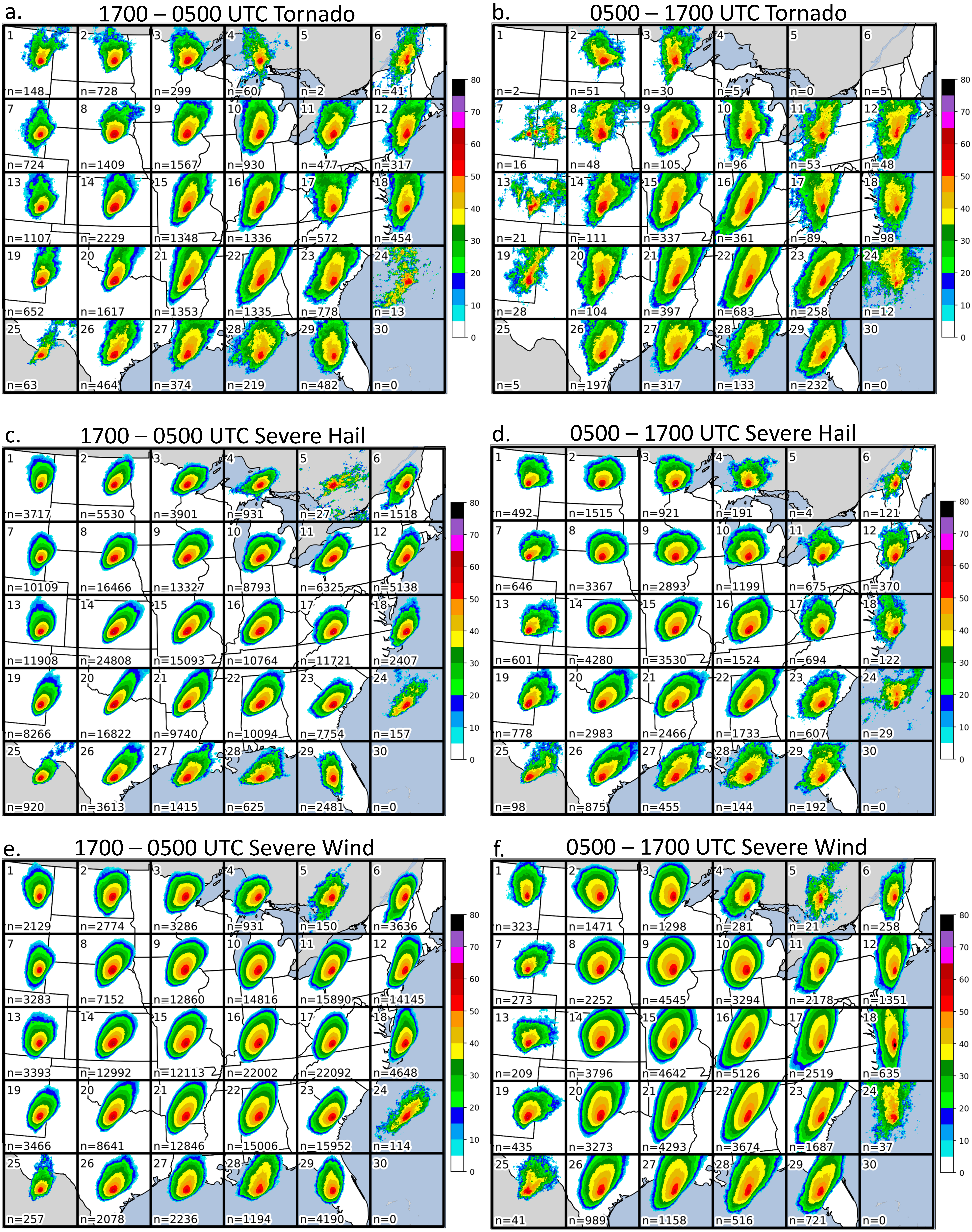
a. 1700 – 0500 UTC Tornado
1 n=148
2 n=728
3 n=299
4 n=60
5 n=2
6 n=41
7 n=724
8 n=1409
9 n=1567
10 n=930
11 n=477
12 n=317
13 n=1107
14 n=2229
15 n=1348
16 n=1336
17 n=572
18 n=454
19 n=652
20 n=1617
21 n=1353
22 n=1335
23 n=778
24 n=13
25 n=63
26 n=464
27 n=374
28 n=219
29 n=482
30 n=0
b. 0500 – 1700 UTC Tornado
1 n=2
2 n=51
3 n=30
4 n=5
5 n=0
6 n=5
7 n=16
8 n=48
9 n=105
10 n=96
11 n=53
12 n=48
13 n=21
14 n=111
15 n=337
16 n=361
17 n=89
18 n=98
19 n=28
20 n=104
21 n=397
22 n=683
23 n=258
24 n=12
25 n=5
26 n=197
27 n=317
28 n=133
29 n=232
30 n=0
c. 1700 – 0500 UTC Severe Hail
1 n=3717
2 n=5530
3 n=3901
4 n=931
5 n=27
6 n=1518
7 n=10109
8 n=16466
9 n=13327
10 n=8793
11 n=6325
12 n=5138
13 n=11908
14 n=24808
15 n=15093
16 n=10764
17 n=11721
18 n=2407
19 n=8266
20 n=16822
21 n=9740
22 n=10094
23 n=7754
24 n=157
25 n=920
26 n=3613
27 n=1415
28 n=625
29 n=2481
30 n=0
d. 0500 – 1700 UTC Severe Hail
1 n=492
2 n=1515
3 n=921
4 n=191
5 n=4
6 n=121
7 n=646
8 n=3367
9 n=2893
10 n=1199
11 n=675
12 n=370
13 n=601
14 n=4280
15 n=3530
16 n=1524
17 n=694
18 n=122
19 n=778
20 n=2983
21 n=2466
22 n=1733
23 n=607
24 n=29
25 n=98
26 n=875
27 n=455
28 n=144
29 n=192
30 n=0
e. 1700 – 0500 UTC Severe Wind
1 n=2129
2 n=2774
3 n=3286
4 n=931
5 n=150
6 n=3636
7 n=3283
8 n=7152
9 n=12860
10 n=14816
11 n=15890
12 n=14145
13 n=3393
14 n=12992
15 n=12113
16 n=22002
17 n=22092
18 n=4648
19 n=3466
20 n=8641
21 n=12846
22 n=15006
23 n=15952
24 n=114
25 n=257
26 n=2078
27 n=2236
28 n=1194
29 n=4190
30 n=0
f. 0500 – 1700 UTC Severe Wind
1 n=323
2 n=1471
3 n=1298
4 n=281
5 n=21
6 n=258
7 n=273
8 n=2252
9 n=4545
10 n=3294
11 n=2178
12 n=1351
13 n=209
14 n=3796
15 n=4642
16 n=5126
17 n=2519
18 n=635
19 n=435
20 n=3273
21 n=4293
22 n=3674
23 n=1687
24 n=37
25 n=41
26 n=989
27 n=1158
28 n=516
29 n=721
30 n=0
0 10 20 30 40 50 60 70 80

Mean Storms: Composites of Radar Reflectivity Images During Two Decades of Severe Thunderstorm Events

ALEX M. HABERLIE*, WALKER S. ASHLEY, MARISA R. KARPINSKI

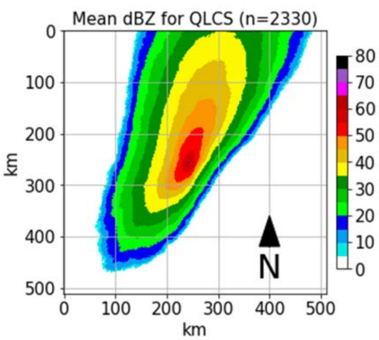

Weather radar image archives provide a rich repository of storm intensity proxies that have been used in many climate studies. We describe a method for illustrating the mean spatial structures of storm intensity around half a million severe thunderstorm reports. The resulting mean storm structures vary greatly between regions, time of day, time of year, and affirms existing studies. This dataset will also provide a method for researchers to benchmark new approaches in image classification and storm mode identification.